PNNL- 28383

Prepared for the U.S. Department of Energy
under Contract DE-AC05-76RL01830

Pacific Northwest
NATIONAL LABORATORY

Proudly Operated by Battelle Since 1965

Carbide Particle Redistribution in U-10Mo Alloy during Hot Rolling Process

Synthetic Microstructure-Based Finite-Element Approach

December 2018

KS Choi
C Wang
C Lavender
VV Joshi

U.S. DEPARTMENT OF
ENERGY

DISCLAIMER

PACIFIC NORTHWEST NATIONAL LABORATORY
operated by
BATTELLE
for the
UNITED STATES DEPARTMENT OF ENERGY
under Contract DE-AC05-76RL01830

Printed in the United States of America

Available to DOE and DOE contractors from the Office of Scientific and Technical Information,
P.O. Box 62, Oak Ridge, TN 37831-0062
www.osti.gov
ph: (865) 576-8401
fax: (865) 576-5728
email: reports@osti.gov

Available to the public from the National Technical Information Service
5301 Shawnee Rd., Alexandria, VA 22312
ph: (800) 553-NTIS (6847)
or (703) 605-6000
email: info@ntis.gov
Online ordering: http://www.ntis.gov

PNNL- 28383

Carbide Particle Redistribution in U-10Mo Alloy during Hot Rolling Process

Synthetic Microstructure-Based Finite-Element Approach

KS Choi
C Wang
C Lavender
VV Joshi

December 2018

Prepared for
the U.S. Department of Energy
under Contract DE-AC05-76RL01830

Pacific Northwest National Laboratory
Richland, Washington 99354

Summary

The influence of initial carbide particle distribution features on the evolution of particle and stringer distribution within U-10Mo alloy during hot rolling was investigated in this study. This work will provide guidance to casting optimization work and identify actionable process changes to eliminate the surface features directly attributed to carbides. Various synthetic microstructure-based finite-element (FE) models were generated with consideration of different parameters (i.e., particle shape, particle volume fraction and particle distribution). Plane-strain compression loading was employed in the FE models to simulate hot rolling to 40% and 80% reductions. Stringer statistics analyses and two-point correlation functions were then performed with the simulated hot-rolling results.

The results from stringer analyses show that stringer volume fraction substantially increases with increased rolling reduction for microstructure with particles distributed along grain boundaries, and that microstructures with elliptical particles may have slightly higher stringer volume fractions than those with circular particles. The results also show that the maximum stringer length can increase substantially with increased rolling reduction for microstructures with elliptical particles along grain boundaries, and that the microstructures with higher-aspect-ratio elliptical particles may have higher stringer volume fraction and higher maximum stringer length. Near-surface numbers of particles and particle volume fractions also increase with increased rolling reduction. The results from application of the two-point correlation function show that the particle shape (i.e., circular or elliptical) may not have significant influence on the overall shapes of the correlation curves, and that the correlation curves tend to show higher peaks at short distance and then gradually decrease for microstructures with higher particle volume fractions and particles distributed along grain boundaries.

Acknowledgments

This work was supported by the U.S. Department of Energy's National Nuclear Security Administration. The authors would like to acknowledge Drs. Xiaohua Hu and Guang Cheng, who were previously Pacific Northwest National Laboratory (PNNL) staff members, for their preliminary contributions to this work.

Acronyms and Abbreviations

2PCF	two-point correlation function
FE	finite-element
HIP	hot isostatic pressing
LEU	low-enriched uranium
Mo	molybdenum
PNNL	Pacific Northwest National Laboratory
PVF	particle volume fraction
SEM	scanning electron microscopy
SVF	stringer volume fraction
U-10Mo	uranium alloy with ten weight percent molybdenum (22 atomic percent Mo)
U-Mo	uranium-molybdenum
wt%	weight percent

Contents

Figures

Tables

1.0 Introduction

Since the 1980s, the U.S. Department of Energy's United States High Performance Research Reactor (USHPRR) Conversion Program has investigated low-enriched uranium (LEU) as an alternative to high-enriched uranium. Because of its high density and favorable performance during fabrication and irradiation, uranium alloyed with 10 wt% molybdenum (U-10Mo) has been identified as the most promising candidate LEU fuel [1-3]. U-10Mo alloy fabrication involves a complex series of material processing steps, including casting, homogenization, hot roll bonding of a zirconium interlayer, cold rolling, annealing, and hot isostatic pressing (HIP) [4, 5]. Various analysis and modeling methods have been developed for many of these individual processes [6-9]

Generally, the as-cast U-10Mo alloys include second-phase carbide particles in their matrix region. Hot rolling and cold rolling are then performed to reduce the thickness of as-cast alloys, improve their strength, and optimize their microstructures. During such processing, the particles in the initial microstructures are likely to align along the rolling direction and form clustered particles, or stringers. The stringers or stringer-type particle clusters provide a possible propagation path for cracks or fractures, which reduces the material's resistance to damage [10, 11].

Hu et al. [12-14] studied the correlation between particle volume fraction (PVF), stringer volume fraction (SVF), and stringer length in aluminum alloys by generating microstructure-based finite-element (FE) models, and they elucidated the effects of stringers on the local fracture strain. Recently, Cheng et al. [10] investigated the effect of secondary carbide particles and stringers on the microstructural evolution of U-10Mo alloys after rolling and recrystallization using actual microstructure-based FE models. Six material samples were selected for their study, which may not provide enough information on the influence of particle distribution features on the microstructural evolution during rolling.

As presented in Cheng et al. [10], the particle size, distribution, and volume fraction in U-10Mo alloys can be quite different depending on the employed thermomechanical process, and it is expected that the final carbide particle distributions can have direct effects on the fuel performance. It is therefore important to control the particles in the initial microstructures to obtain the desired material performance after hot rolling [15-19]. In order to obtain the desired initial microstructures, we need to have fundamental understanding of the general influence of initial microstructural features on the microstructural evolution during subsequent fabrication processes.

In this report, the influence of initial carbide particle distribution features on the evolution of particle distribution and stringer distribution within U-10Mo alloy during hot rolling is investigated using synthetic microstructure-based FE models. For this purpose, the average of carbide particle size distribution was first determined from analyses of three actual U-10Mo alloy samples. With the obtained particle size distribution, various synthetic microstructure-based FE models were then generated with consideration of additional parameters (i.e., PVF, particle shapes, and particle distributions). Plane-strain compression loading was employed in the FE models to simulate the hot rolling process down to 40% and 80% reductions. Stringer statistics analyses and two-point correlation functions (2PCFs) were then performed on the simulated results. SVFs, maximum stringer lengths, and 2PCF curves were compared among the models with different initial microstructural features. Evolution of near-surface particle distributions during rolling were also examined. Finally, conclusions based on the results of these investigations were made and future work is also presented.

2.0 Finite-Element Modeling

2.1 Model Description

Three different U-10Mo samples with varied carbide particle concentrations, distributions, and sizes were used in this study to obtain the average features of the particle size and its distribution. Figure 1 shows scanning electron microscopy (SEM) images of the three samples; each image presents a 1200 μm (width) by 900 μm (height) region in the as-cast and homogenized alloys [10, 20]. The bright regions are the individual U-10Mo grains and the dark spots are carbide particles. As shown in the figure, the volume fractions, sizes, morphologies, and distributions of particles are quite different among the samples because of the different heat treatment parameters and compositions of the samples. Image analyses, based on in-house MATLAB codes, were conducted to calculate the particle size distributions within the three samples. Figure 2 shows the particle size distributions in the form of probability density functions. As shown in the figure, the samples appeared to show similar particle size distributions: small-sized particles (i.e., *radius* < ~3 μm) are quite dominant, with much lower probability of large-sized particles. The calculated particle size distributions were approximated using the log-normal distribution that is defined in Equation (1):

$$f(x \mid \mu, \sigma) = \frac{1}{x\sigma\sqrt{2\pi}} \exp\left(\frac{-(\ln x - \mu)^2}{2\sigma^2}\right) \tag{1}$$

where

$$\mu = \ln\left(\frac{m}{\sqrt{1+\frac{v}{m^2}}}\right) \tag{2}$$

$$\sigma^2 = \ln\left(1 + \frac{v}{m^2}\right) \tag{3}$$

Here, m and v can denote the mean and variance of the particle radius values. The log-normal distribution with m = 1.7, v = 1 is also plotted in Figure 2, and captures well the overall particle size distribution features of the three samples. The detailed processing/history of the samples can be found in the report by Nyberg et al. [19, 21].

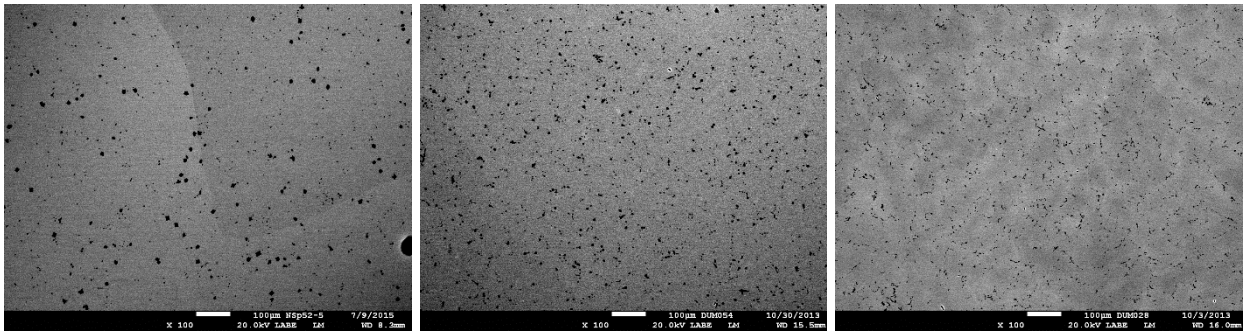

(a) (b) (c)

Figure 1. SEM images showing the initial as-cast and homogenized microstructures of three samples: (a) Sample 1, (b) Sample 2, and (c) Sample 3.

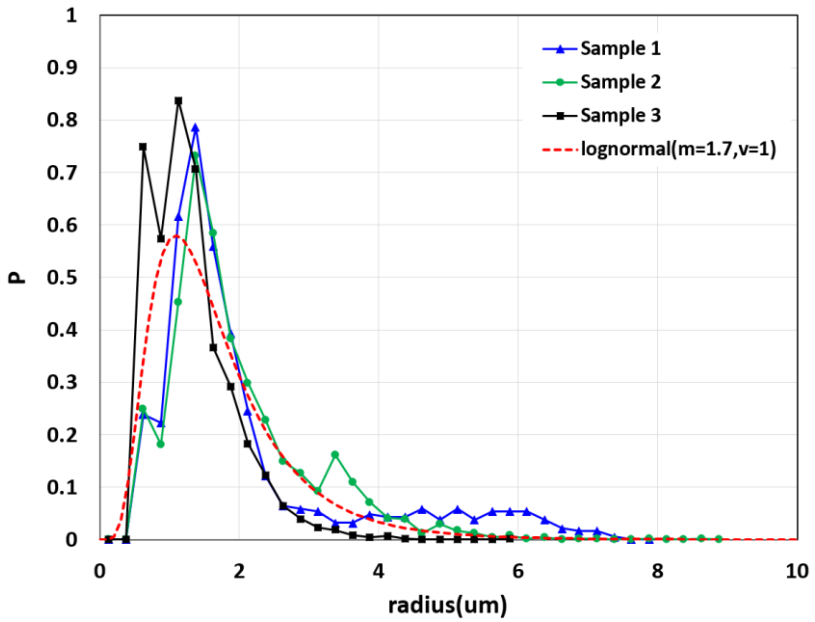

Figure 2. Actual particle size distributions in the three samples compared to a log-normal distribution.

With the approximated particle size distribution (i.e., log-normal distribution with m = 1.7, v = 1), additional parameters are also considered in generating synthetic microstructures. As listed in Table 1, three different PVFs (0.5, 1.0, and 2.0 %), two different particle shapes (circular and elliptical), and two different particle distributions (random and along grain boundaries) are considered in this study. Twelve different microstructural features can be generated based on the variations of parameters listed in Table 1. A MATLAB code was developed to generate the synthetic microstructures based on the features in the table.

Figure 3 shows the particle size distribution adopted in generating the synthetic microstructures. As shown in the figure, the particle size followed the same log-normal distribution as approximated in Figure 2, and the particle radius was bounded between 1 μm and 9 μm. Actual grain boundary information was also needed for generating the synthetic microstructures with particles along grain boundaries. Figure 4 shows the actual grain structures of a U-10Mo sample; this image was used for extracting the information on grain boundaries and their directions. The extracted information was then applied for seeding the particles along the grain boundaries.

Table 1. Model description for synthetic microstructure-based models.

Parameter	Variation
Initial model size	1182 × 887 μm^2 (pixels)
Particle volume fraction (PVF)	0.5%, 1.0%, 2.0%
Particle size distribution	log-normal distribution (m = 1.7, v = 1)
Particle shape	Circle, ellipse
Particle distribution	Random, along grain boundaries

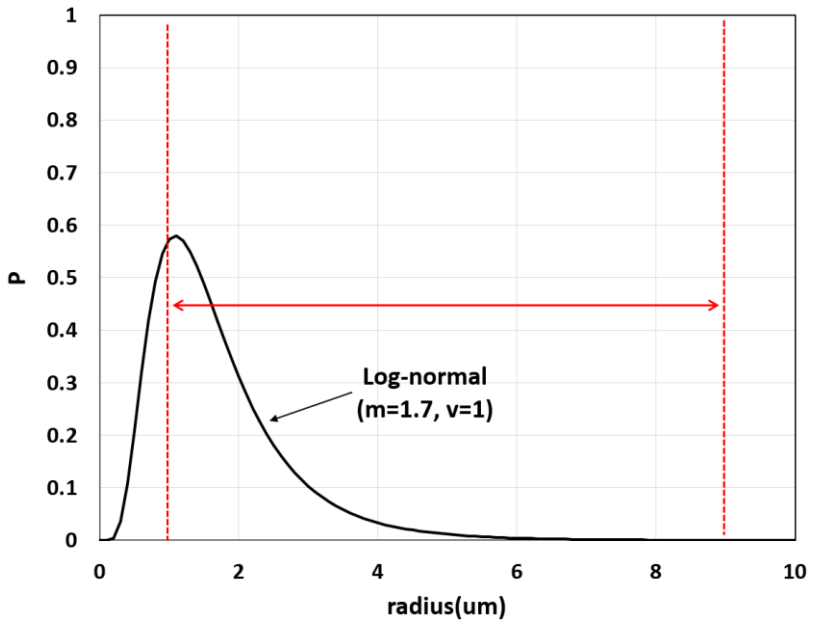

Figure 3. Log-normal distribution and bounds of particle size used in generating synthetic microstructure-based models.

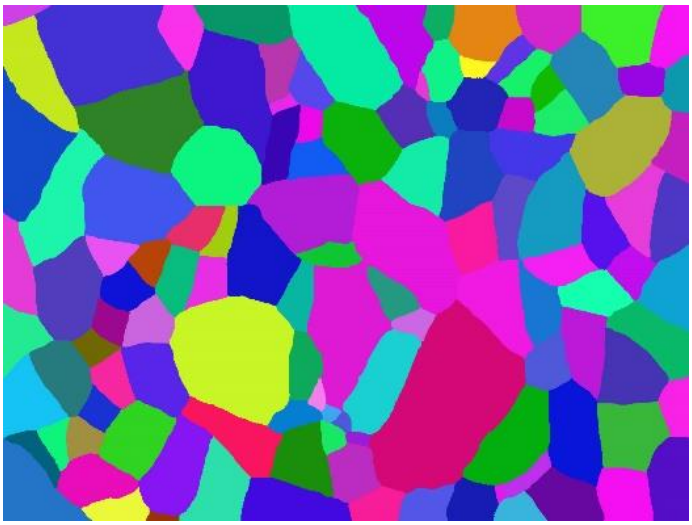

Figure 4. The image used for extracting the grain boundary information.

2.2 Synthetic Microstructure-Based Models

Figure 5 and Figure 6 are examples of the generated synthetic microstructures with the twelve different microstructural features listed in Table 1. The size of all the microstructures in the figures is 1182 × 887 μm^2 (pixels) as noted in Table 1. Figure 5 shows the microstructures with random particle distributions with three different PVFs (i.e., 0.5%, 1.0%, and 2.0%) for circular and elliptical particles. Figure 6 shows the microstructures with the particles along the grain boundaries with three different PVFs (i.e., 0.5%, 1.0%, and 2.0%) for circular and elliptical particles. Note here that, for the microstructures with the elliptical particles, about 30% of the particles are circular while the others are elliptical with the aspect ratio of 1~2, and the grain boundary directions shown in Figure 4 were used to assign the directions of major axes of the elliptical particles. It can also be seen in Figure 5 and Figure 6 that the microstructures

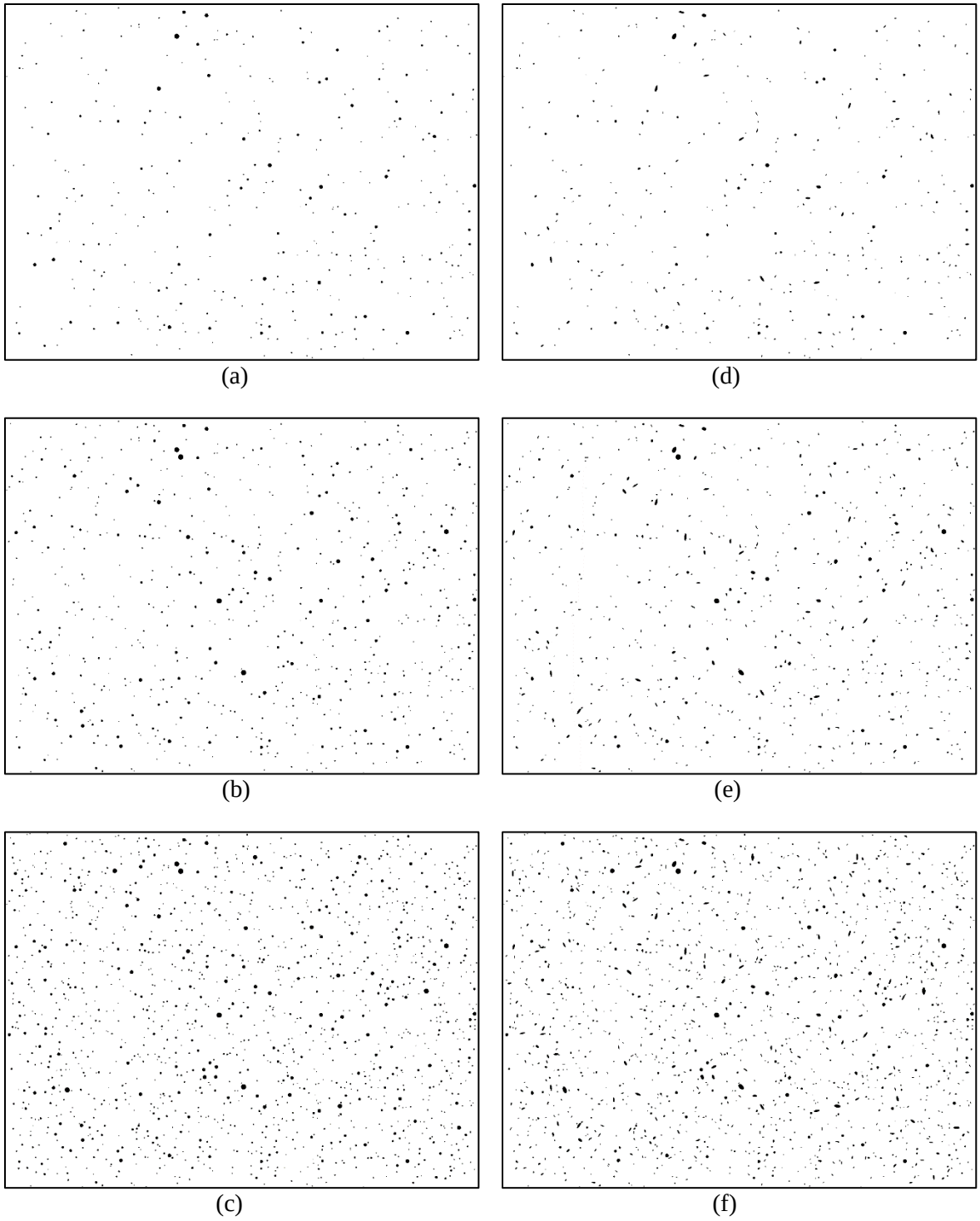

Figure 5. Examples of synthetic microstructures with random particle distributions: (a), (b), (c) circular particles with 0.5%, 1.0%, and 2.0% PVF, respectively, and (d), (e), (f) elliptical particles with 0.5%, 1.0%, and 2.0% PVF, respectively.

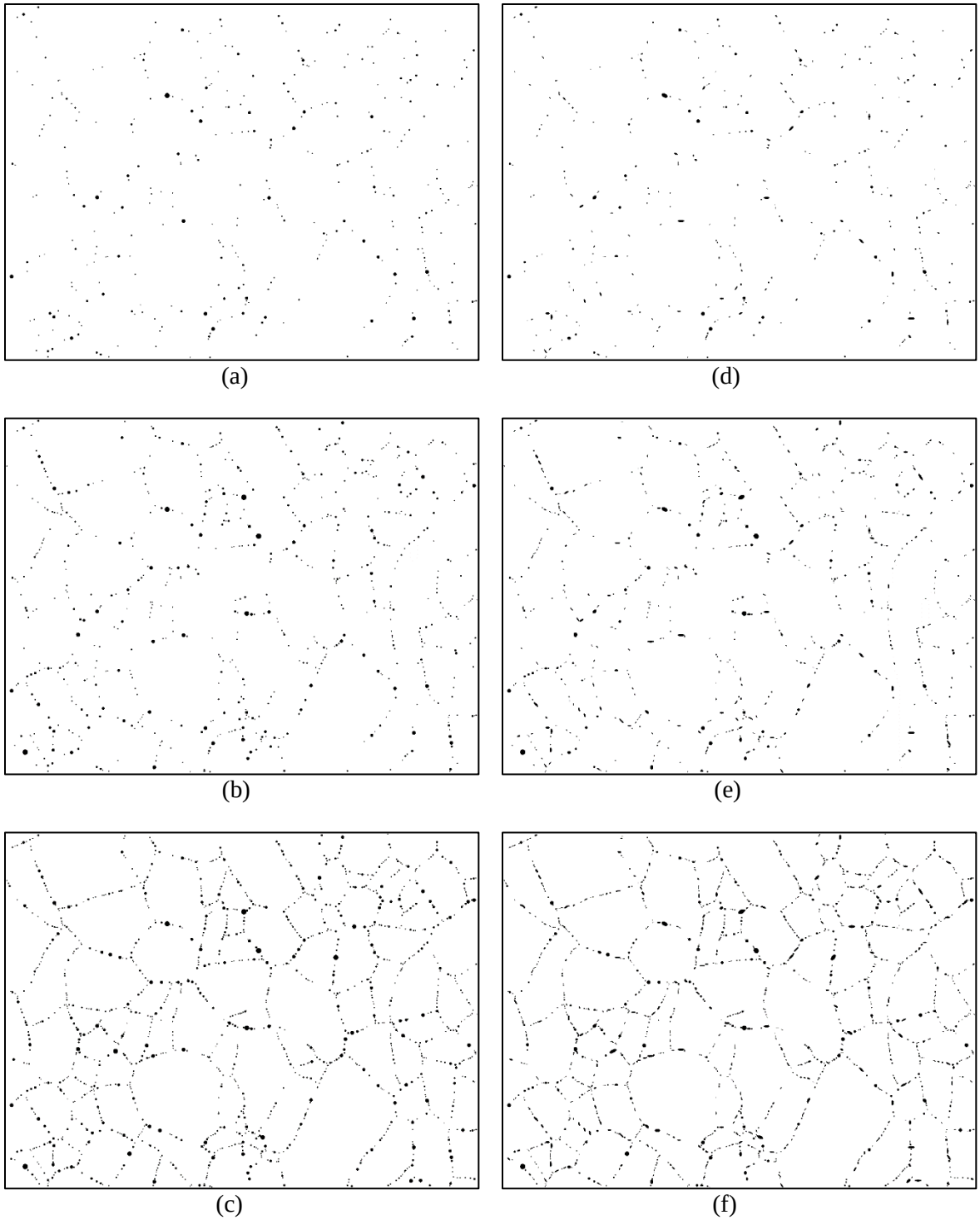

Figure 6. Examples of synthetic microstructures with particles distributed along grain boundaries: (a), (b), (c) circular particles with 0.5%, 1.0%, and 2.0% PVF, respectively, and (d), (e), (f) elliptical particles with 0.5%, 1.0%, and 2.0% PVF, respectively.

with elliptical particles have exactly the same particle distributions (i.e., locations) as those of the corresponding microstructures with circular particles. This way, it is expected that the pure effects of particle shape on the evolution of particle distribution during hot rolling can be better investigated. In this study, five different microstructures were generated for each microstructural feature in order to obtain average results for each feature.

2.3 Hot Rolling Simulation

Simple plane-strain compression simulation was used in a recent study of the evolutions of particle distribution during multi-pass hot rolling of an annealed U-10Mo coupons [10, 20]. All the generated microstructures shown in Figure 5 and Figure 6 were converted to plane-strain FE models. Each pixel (1 × 1 μm^2) in a microstructure image was represented by one element in the FE models. The commercial FE code ABAQUS/Explicit was used for the simulations in this study. A multipoint constraint was applied to keep the right and left edges of the model straight vertically during the compression (i.e., rolling) process. The flow behavior of the matrix material was assumed to be isotropic with an elastic modulus of 65 GPa; the flow curve adopted in the simulation is presented in Figure 7 [20]. The particles were assumed to be purely elastic and only the elastic modulus of 225 GPa was used in the simulation.

In this study, simulations for two-step rolling reductions (i.e., 40% and 80%) were conducted. Possible fracture of the particles was not considered in the simulations, as the samples were assumed to undergo hot rolling. After the first 40% rolling reduction from the initial microstructure, the resulting microstructures (~1967 × 532 μm^2) with the redistributed particles were remeshed using 1 × 1 μm^2 elements for the next-step rolling simulation. The samples after 40% rolling reduction were assumed to undergo an annealing treatment and become free of any internal residual stresses. Therefore, the same flow stress curve shown in Figure 7 could also be adopted in the second rolling from 40% to 80% rolling reduction. After 80% rolling reduction, the resulting microstructures (~5785 × 178 μm^2) were also remeshed using 1 × 1 μm^2 elements for the purpose of particle distribution analysis. Note that, for most of the microstructures with large PVF (i.e., ~2%), the second rolling simulations (i.e., 40% to 80%) could not be completed in a single step due to severe mesh distortions in matrix regions between the carbide particles. For these microstructures with large PVFs, remeshing the intermediate microstructure at ~70%

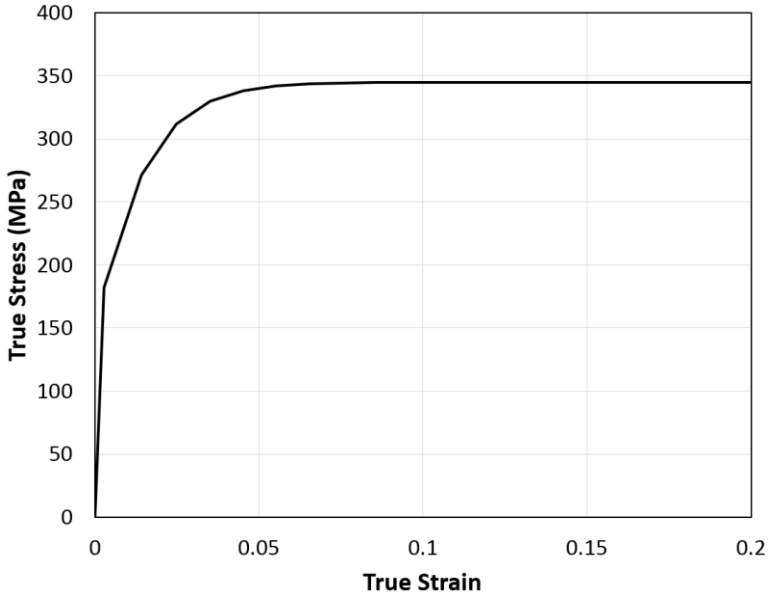

Figure 7. Flow curve used for U-10Mo matrix material during hot rolling.

rolling reduction was conducted to bypass the mesh distortion issues, and then a third rolling simulation from ~70% to 80% reduction could be performed. It is pointed out here that, when the intermediate microstructures at ~70% rolling reduction were remeshed, the equivalent plastic strain distributions in matrix regions were also interpolated and calculated for the remeshed elements. These newly calculated

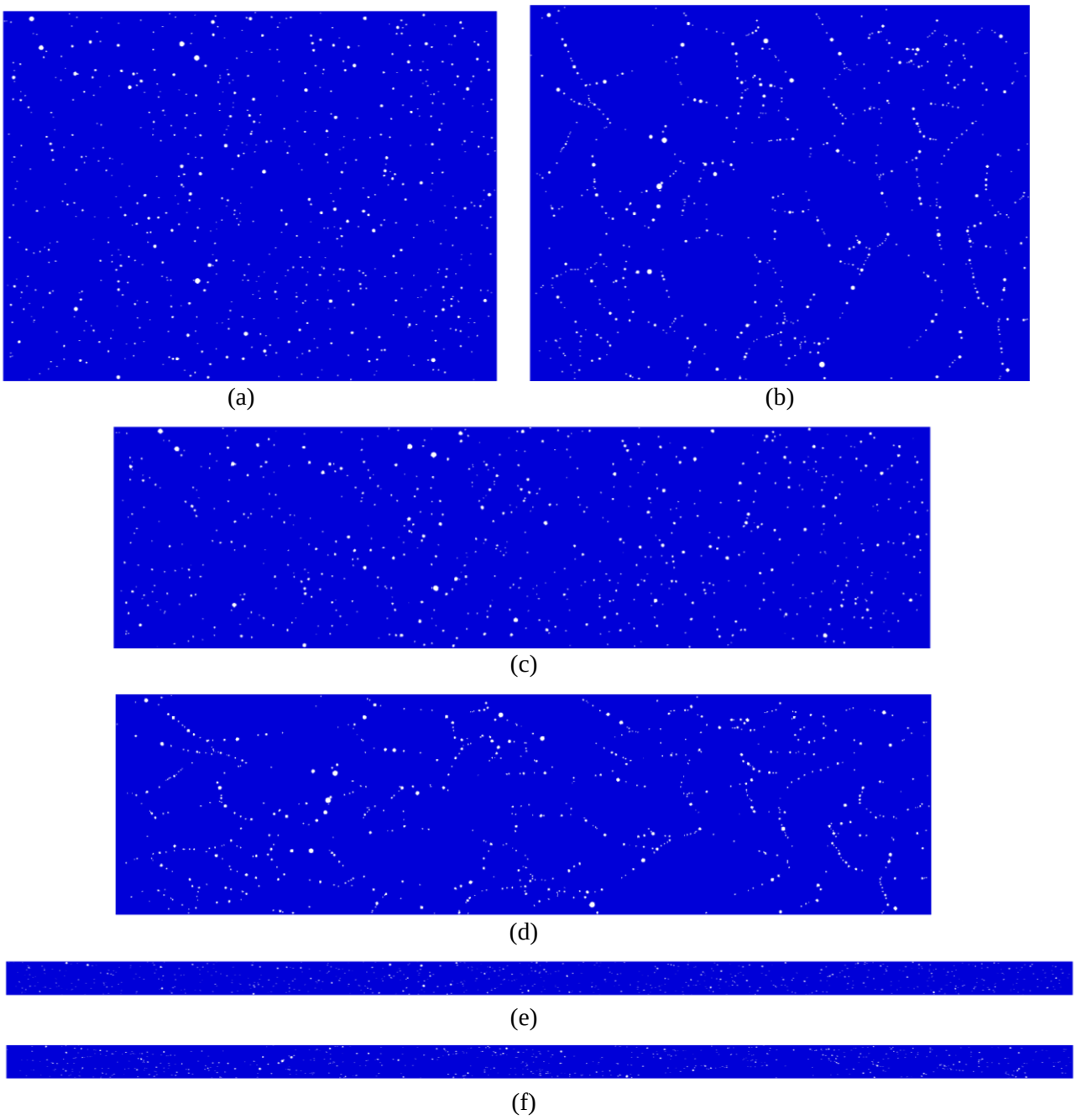

Figure 8. Particle distributions in the example models with circular particles and PVF of 1%: (a), (c), (e) random particle distribution for initial condition (1182 × 887 μm^2), and after 40% (1967 × 532 μm^2) and 80% (5785 × 178 μm^2) rolling reductions, respectively; (b), (d), (f) particle distribution along grain boundaries for initial condition (1182 × 887 μm^2), and after 40% (1967 × 532 μm^2) and 80% (5785 × 178 μm^2) rolling reductions, respectively.

equivalent plastic strain distributions had to be used as the initial conditions for the simulations of the third rolling reduction since an annealing treatment is not assumed at ~70% rolling reduction.

Figure 8 shows the particle distributions after each rolling process in example models with circular particles and 1% PVF for random particle distribution and particle distribution along grain boundaries. As shown in the figure, with progressive rolling reduction, these carbide particles redistribute and tend to align as stringers along the rolling direction. It is well known that the redistribution of carbides can influence the recrystallization during annealing treatment. The recrystallization of multiple grains is not in the scope of this study. In order to better understand the influence of different microstructural features and rolling reductions on the evolution of particle distribution, it is important to obtain statistical analysis of the particle distributions for different microstructures undergoing rolling reductions.

3.0 Results and Discussion

3.1 Carbide Particle Distribution Analysis

As mentioned above, carbide particles redistribute with progressive rolling, and tend to align as stringers along the rolling direction. The influence of different microstructural features on the evolution of particle distribution with rolling process is of interest in this study. For this purpose, two major statistical analyses have been performed here: (1) the stringer statistical analyses and (2) 2PCFs. As the stringer evolution is of more interest in this study, this section is focused on discussing the results of stringer analyses. The results of 2PCFs will be introduced in Appendix section.

3.1.1 Stringer Evolution during Hot Rolling

The stringers or stringer-type particle clusters provide a possible propagation path for cracks or fractures, which lowers the damage resistance ability of the materials [10, 11]. It is therefore important to control the particles in the initial microstructures to obtain the desired material performance after hot rolling. In this study, the effects of different microstructural features on their SVF and stringer length are examined.

A stringer identification criterion was determined in previous studies using post-necking modeling [10, 20]. The criterion is briefly introduced here. Each particle within the microstructures was approximated by an ellipse, as shown in Figure 9(a), using a MATLAB code, as follows. First, the coordinates of the center point for the ellipse were calculated by averaging the coordinates of all points (i.e., pixels) in the particle. The major axis was then determined by the two points within the particle that have the longest distance between them. The rotated angle (i.e., angle between the major axis and the horizontal axis) was also calculated using the two points with the largest separation (i.e., longest distance). The length of the minor axis was then calculated by dividing the area of the particle by the length of the major axis. For the purpose of identifying a stringer, as shown in Figure 9(b), a line was first drawn to connect the center points of two particles. The angle between the connecting line and the horizontal direction is defined as θ, the line segments within particle 1 and particle 2 are defined as r_1 and r_2, respectively, and the distance between the two particle centers is defined as d. The angles for angular misalignment between the particles are kept the same as those in ASTM E45-05 at 10° [22]. Because the critical distance d between two particles was estimated as 5 times the sum of the two radii, the stringer identification criterion can be defined as follows:

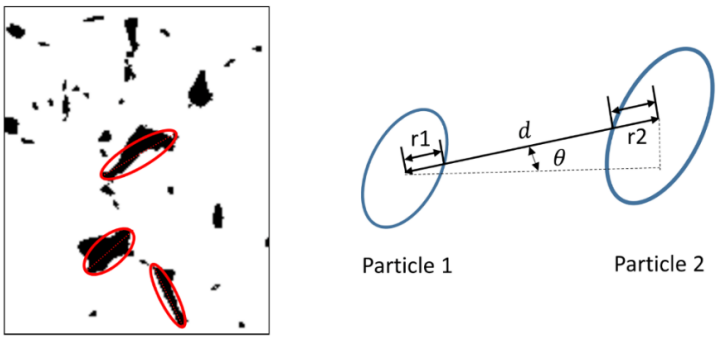

Figure 9. (a) A sketch showing the approximation of particles using ellipses and (b) a sketch of stringer identification criteria used in this study.

$$\theta \leq 10° \tag{4}$$

$$d \leq 5 * (r_1 + r_2) \tag{5}$$

If two particles are found to satisfy the criterion listed above, that pair of particles is considered a two-particle stringer. After the criterion above is applied to all the particles within the microstructure, all the two-particle stringers can be identified, and a list of two-particle stringers with the particle labels is then obtained. Note that, if one particle is found in different two-particle stringer pairs, the list is to be adjusted by merging two-particle stringers that include the same particle. Thus, a new stringer list, including three or more particles, can be finally obtained.

Stringer analyses were conducted for all the initial microstructures with different features as well as the corresponding deformed microstructures after 40% and 80% rolling reduction. Note that, similar to the application of 2PCF, stringer analyses were also conducted with the remeshed microstructure data (i.e., 1967 × 532 pixels and 5785 × 178 pixels) after rolling reduction. Figure 10 shows example results of stringer analysis. The microstructure here is deformed by 40% rolling reduction and has 2% PVF of circular particles along the grain boundary, as shown in Figure 10(a). Figure 10(b) shows the distribution of particles that were identified as stringers based on the criterion in Equations ($\theta \leq 10°$ (4) and ($d \leq 5 * (r_1 + r_2)$ (5). The total number of detected stringers is 128, and the calculated SVF is 38.5%. Here, SVF is defined as

$$\text{Stringer volume fraction} = \frac{volume\ faction\ of\ particles\ identified\ as\ stringer}{particle\ volume fraction\ within\ entire\ microstructure} \tag{6}$$

As shown in Figure 10(b), stringers can have different numbers of particles with different lengths. The stringer length here is simply determined as the direct distance between the two particles on both ends of the stringer. Figure 10(c)–Figure 10(j) shows collections of stringers composed of the same number of particles. The number of stringers, SVF, and average/maximum stringer length is also shown beside each panel. For the microstructure in Figure 10, the longest stringer is ~158 μm, comprising 10 particles, as shown in Figure 10(j). Since this maximum-length-stringer (i.e., 10 particles with ~158 μm) is located very close to a six-particle stringer as shown in Figure 10(b), the maximum stringer length may appear to be much more than ~158 μm if the lengths of the two stringers are added. However, from the strict application of the criterion in Equations ($\theta \leq 10°$ (4) and ($d \leq 5 * (r_1 + r_2)$ (5), these two stringers are determined to be separate ones. Note that, in this study, the maximum length of stringers is determined by application of the criterion rather than by visual inspection which may be subjective.

The effects of microstructural features on stringer evolution during rolling are summarized/plotted in Figure 11–Figure 14. The results in these figures represent the average values and deviations of five models that have the same microstructural features. Figure 11 and Figure 12 show the evolution of total SVF with the increase of rolling reduction for different microstructural features. The volume fractions of two-, three-, and four-particle stringers are also plotted as additional information. In Figure 11, the SVFs for the microstructures with random particle distributions remain generally the same (for circular particles) or increase only slightly (for elliptical particles) with the increase of rolling reduction. For the microstructures with elliptical particles, as in Figure 11(d) through Figure 11(f), the particles with high aspect ratios may rotate during the rolling process, and their major axes tend to be aligned along the rolling direction, which increases their chances of being identified as stringers based on the adopted criterion, due to the shorter distance between the neighboring particles. Note that the rotation of circular particles does not affect their chances of being identified as stringers. For lower PVF (e.g., 0.5%), a large rolling reduction (e.g., 80%) can increase the horizontal spaces between the particles, and therefore, some particles identified as stringers at 40% rolling reduction may not meet the stringer criterion at 80% rolling reduction, which leads to a decrease in SVF, as in Figure 11(a). However, for higher PVF with many particles, particles that were not identified as stringers at lower rolling reduction may newly fill in the longer horizontal spaces between the particles as the rolling reduction increases. This can form new stringers despite the disappearance of other stringers, and leads to the constant SVF for higher PVF. In Figure 12, the SVFs for the microstructures with particle distributions along grain boundaries are initially similar to those for random particle distributions before rolling, and then substantially increase with rolling reduction: by ~50% and ~100% with the 40% and 80% rolling reductions, respectively. This is because particles along grain boundaries are closer to one another than randomly distributed particles, and will potentially constitute stringers when the grain boundaries are rotated and aligned along the rolling direction as the rolling reduction increases. For the same reason mentioned above, the SVFs for elliptical particles in Figure 12(d) –Figure 12(f) are slightly larger than those for circular particles in Figure 12(a)–Figure 12(c): 5~10% larger for the 40~80% rolling reduction. Note that the rate of increase (i.e., increment of SVF(%)/increment of rolling reduction(%)) depends on the PVF such that the rate of increase becomes higher as the PVF increases: ~0.1, ~0.2, and ~0.4 for 0.5%, 1.0%, and 2.0% PVF, respectively.

Figure 13 and Figure 14 show the evolution of maximum stringer length with increased rolling reduction for different microstructural features. Average lengths of two-, three-, and four-particle-stringers are also plotted. In the figures, the averaged maximum stringer length (i.e., black curves) generally have large deviations, which indicates the scatteredness of maximum stringer length data. Note that, for one microstructure, its longest stringer can be changed from one to another with rolling, and therefore the maximum stringer length of a microstructure can vary up and down even with increased rolling reduction. For example, while the longest stringer in the 40% rolled microstructure shown in Figure Figure 10 is ~158 μm, the new longest stinger after 80% rolling is found to be ~138 μm, comprising 7 particles, which is different from the ~158 μm-length and 10-particle stringer at 40% rolling. However, the curves for maximum stringer length still show some noticeable trends in the effects of microstructural features. For a microstructure with random particle distribution as in Figure 13, the maximum stringer lengths for elliptical particles are a little longer than those for circular particles. For a reason similar to the case of SVF, elliptical particles are more likely to constitute longer stringers than circular particles. Also, in Figure 13, the maximum stringer length appears to increase slightly with increased rolling reduction. However, this trend is not very clear. For a microstructure with particles distributed along grain boundaries as in Figure 14, the maximum stringer lengths are similar to those for random particle distributions before rolling, and then tend to increase with increased rolling reduction. This tendency of increasing with rolling reduction is more prominent in the microstructures with elliptical particles in Figure 14(d)–Figure 14(f) than in those with circular particles. It can be found from overall observations that, for elliptical particles along grain boundaries, the maximum stringer length increases substantially with increased rolling reduction, whereas for all other microstructural features (i.e., circular or elliptical

particles distributed randomly, or circular particles distributed along grain boundaries), the increase of maximum stringer length with rolling reduction is not very significant.

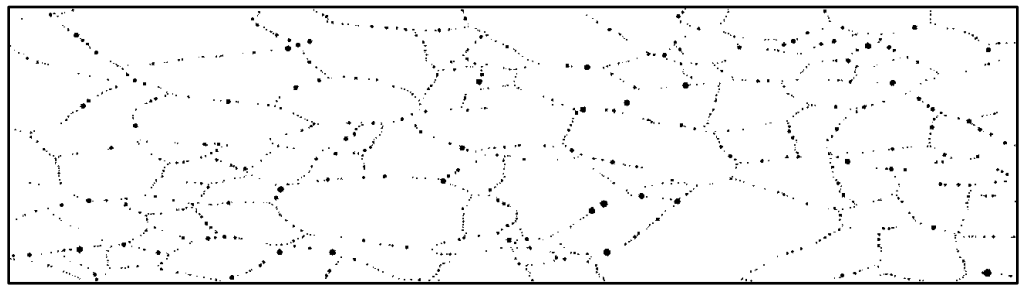

(a)

Circular particles distributed along grain boundaries

PVF: 2%

Reduction: 40%

(b)

Total detected stringers: 128 ea

SVF : 38.5%

Max length:

157.9 µm

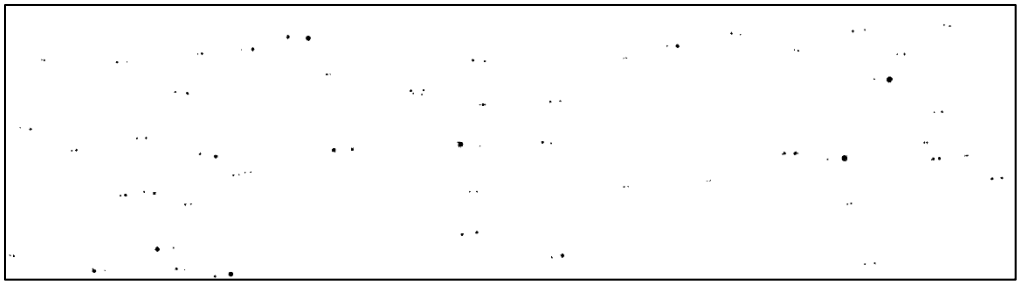

(c)

Two-particle stringers: 51 ea

SVF: 8.1%

Avg/Max length:

17.7/39.8 µm

(d)

Three-particle stringers: 22 ea

SVF: 5.7%

Avg/Max length:

28.3/61.6 µm

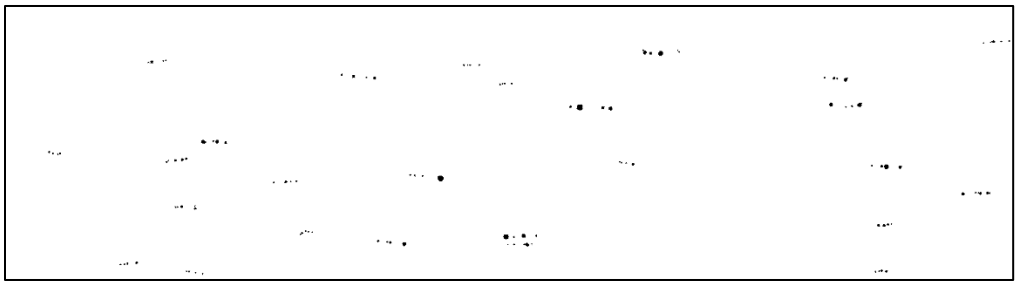

(e)

Four-particle stringers: 26 ea

SVF: 9.2%

Avg/Max length:

42.6/78.4 µm

(f)

Five-particle stringers: 17 ea

SVF: 7.7%

Avg/Max length:

54.5/72.8 µm

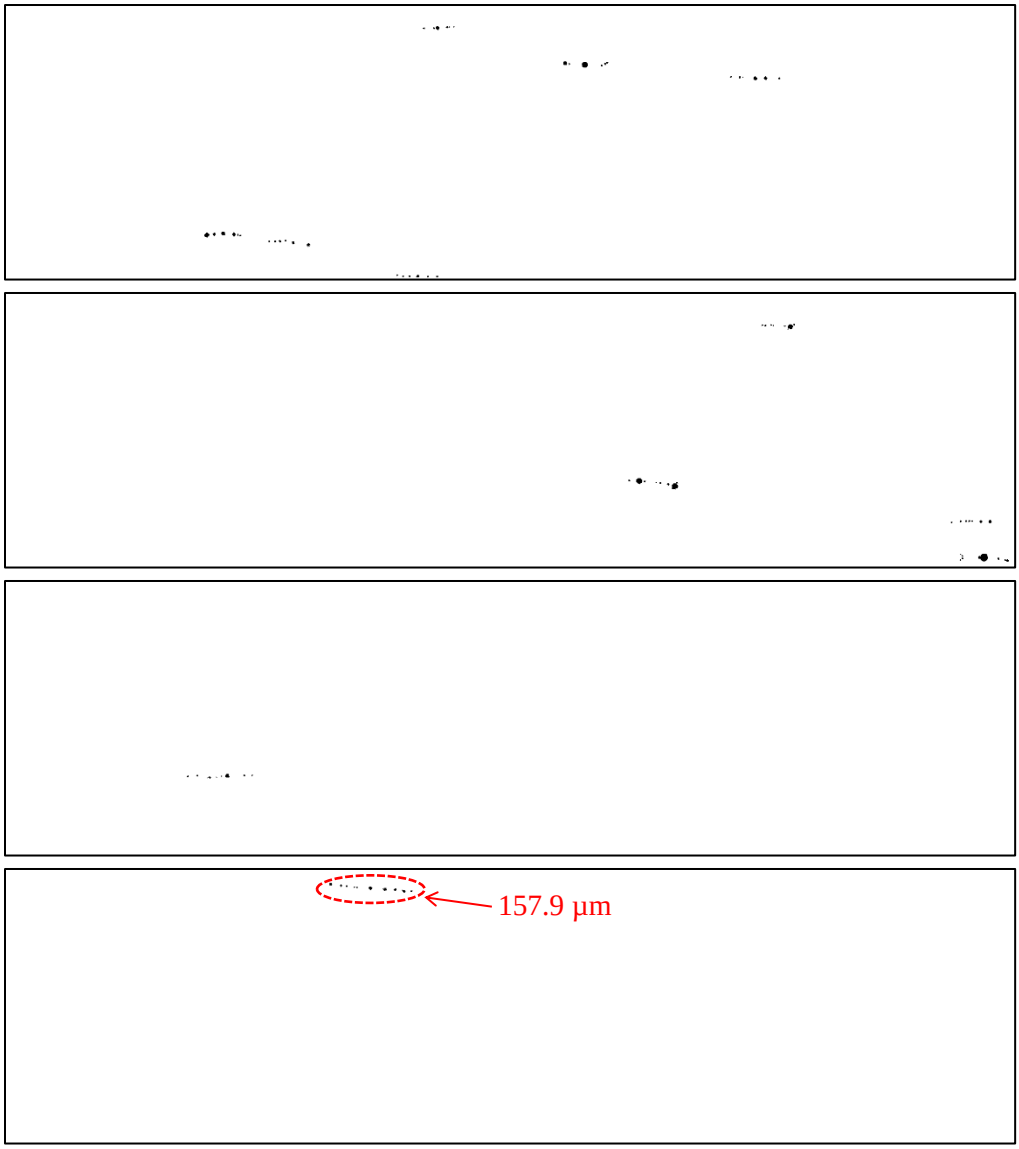

(g)

Six-particle stringers: 6 ea

SVF: 3.3%

Avg/Max length:

75.8/94.4 µm

(h)

Seven-particle stringers: 4 ea

SVF: 3.3%

Avg/Max length:

79.5/90.8 µm

(i)

Eight-particle stringers: 1 ea

SVF: 0.5%

Avg/Max length:

125.7/125.7 µm

(j)

Ten-particle stringers: 1 ea

SVF: 0.8%

Avg/Max length:

157.9/157.9 µm

Figure 10. Example of stringer analysis.

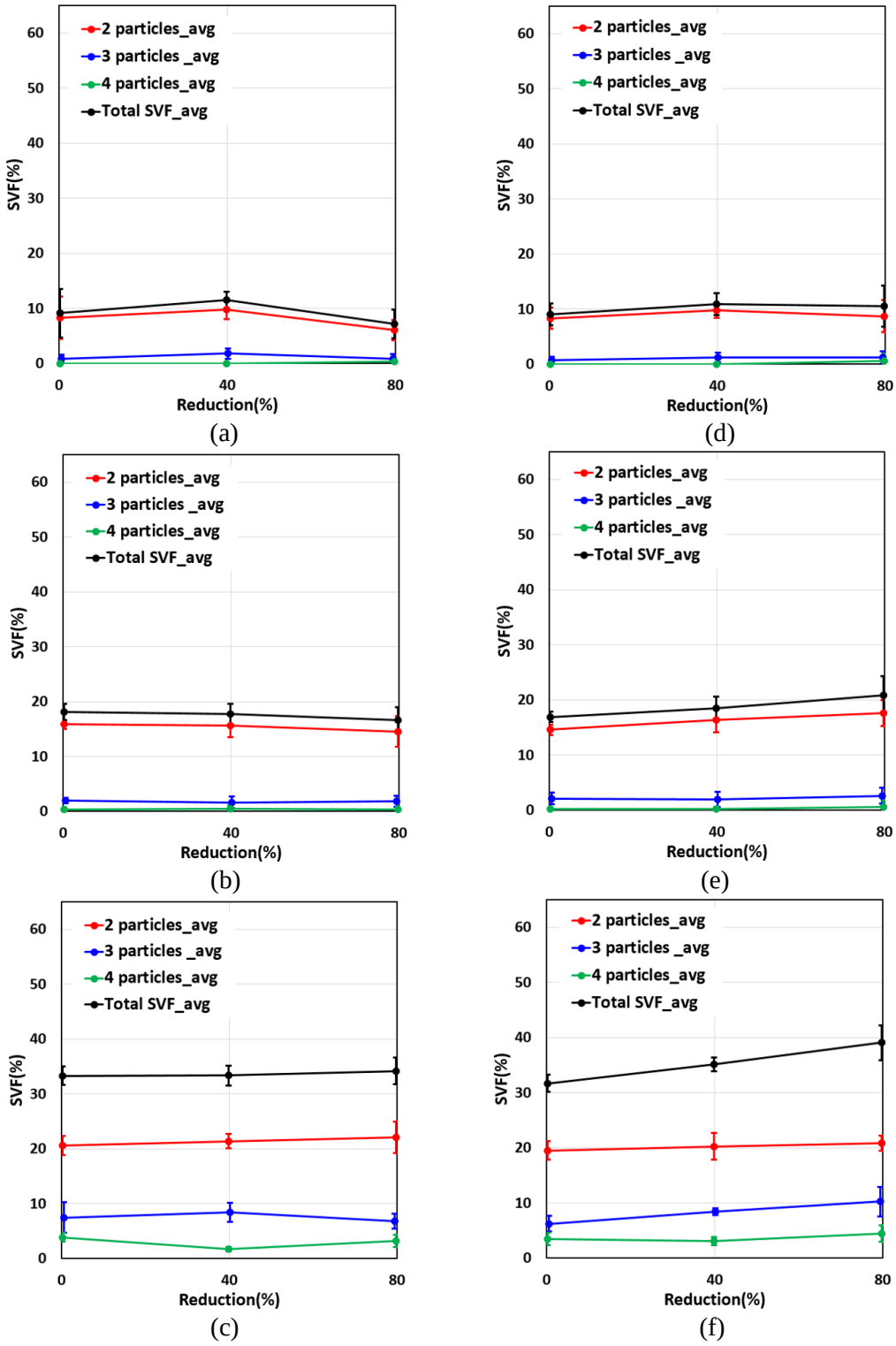

Figure 11. SVFs for random particle distributions: (a), (b), (c) circular particles with 0.5%, 1.0%, and 2.0% PVF, respectively; (d), (e), (f) elliptical particles with 0.5%, 1.0%, and 2.0% PVF, respectively.

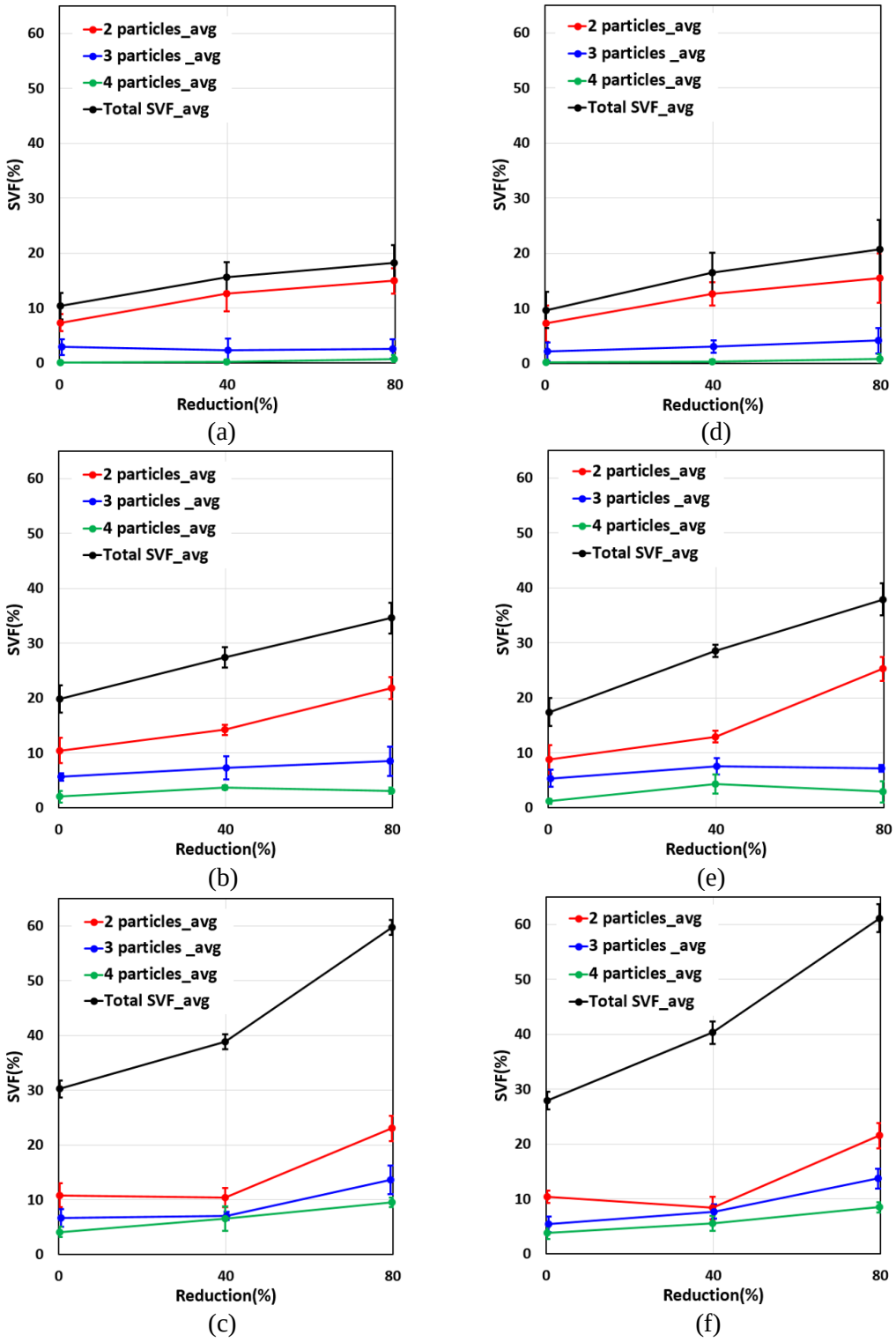

Figure 12. SVFs for particle distribution along grain boundaries: (a), (b), (c) circular particles with 0.5%, 1.0%, and 2.0% PVF, respectively; (d), (e), (f) elliptical particles with 0.5%, 1.0%, and 2.0% PVF, respectively.

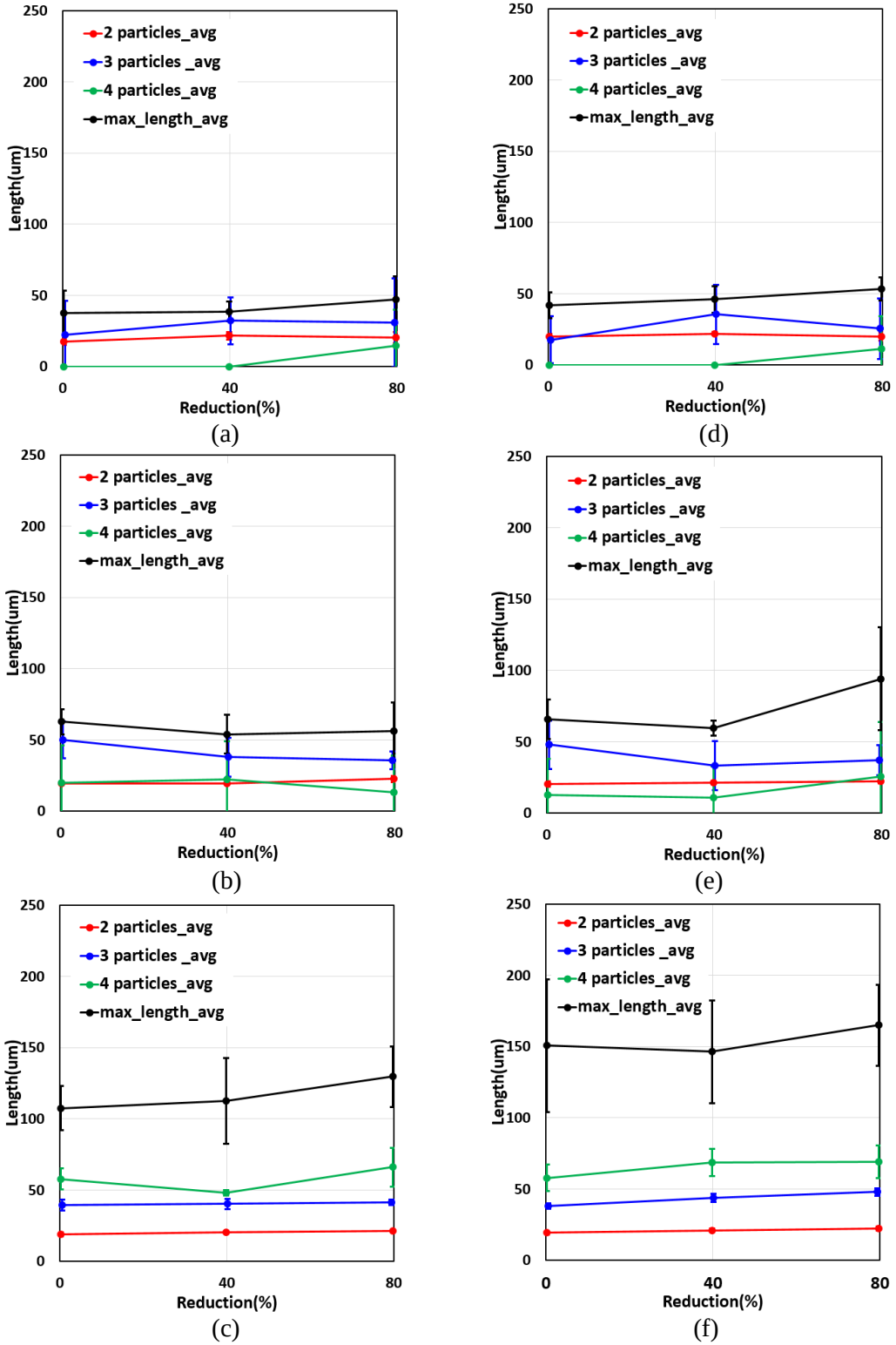

Figure 13. Maximum stringer length for random particle distributions: (a), (b), (c) circular particles with 0.5%, 1.0%, and 2.0% PVF, respectively; (d), (e), (f) elliptical particles with 0.5%, 1.0%, and 2.0% PVF, respectively.

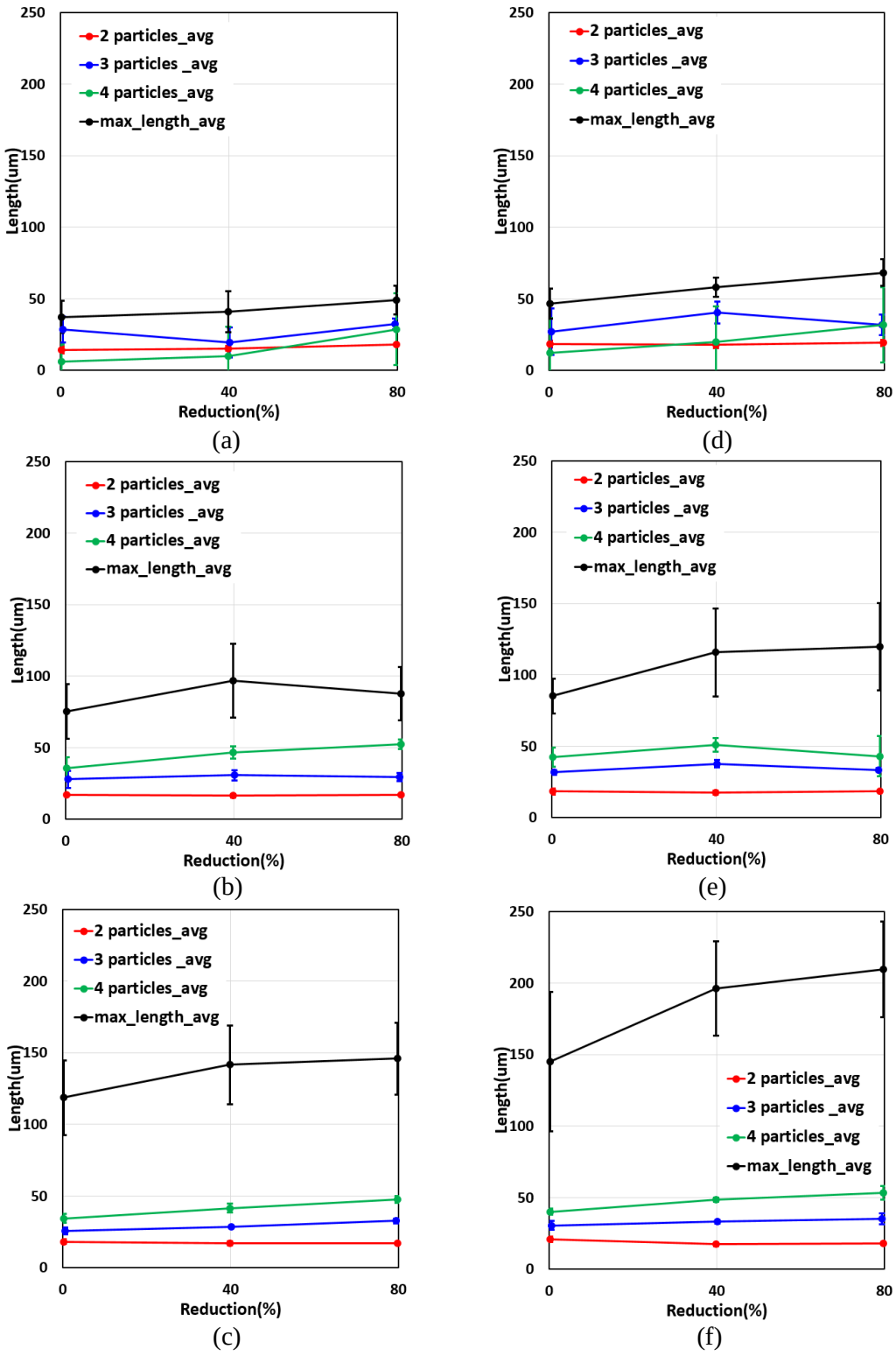

Figure 14. Maximum stringer length for particle distribution along grain boundaries: (a), (b), (c) circular particles with 0.5%, 1.0%, and 2.0% PVF, respectively, and (d), (e), (f) elliptical particles with 0.5%, 1.0%, and 2.0% PVF, respectively.

3.1.2 Effect of Particle Aspect Ratio on Stringer Evolution

The previous section showed that the maximum stringer length increases substantially with increased rolling reduction for distributions of elliptical particles along grain boundaries. Therefore, the effects of aspect ratio of elliptical particles on the maximum stringer length were studied. Five new microstructures with higher-aspect-ratio (i.e., 1~4) elliptical particles distributed along grain boundaries were generated. Here, the aspect ratio 1~4 was selected considering whether the elliptical particles in the generated microstructures have reasonable shapes. Note that, with aspect ratio larger than 4, ellipses tend to be spread across several pixels or touch each other, which may render the results of image processing distorted from reality.

Figure 15 shows a comparison of a previous microstructure with a new microstructure with higher-aspect-ratio elliptical particles, which makes some elliptical particles in the new microstructure very thin and long. Stringer analysis was performed with these new microstructures. The results for SVF and maximum stringer length were compared with those of lower-aspect-ratio elliptical particles. Figure 16 compares the SVFs of the microstructures with lower- and higher-aspect-ratio elliptical particles. For the microstructures with higher-aspect-ratio elliptical particles, the SVF increases a little faster with rolling reduction than that for lower-aspect-ratio elliptical particles, and therefore is larger for all rolling reductions (i.e., 40% and 80%). Note that higher-aspect-ratio elliptical particles have a greater chance of being identified as stringers with increased rolling reduction. Figure 17 compares the maximum stringer lengths of the microstructures with lower- and higher-aspect-ratio elliptical particles. For the microstructures with higher-aspect-ratio elliptical particles, though their maximum stringer length shows a large deviation, the average value is much larger than those for microstructures with lower-aspect-ratio elliptical particles for all conditions (i.e., the initial condition and the 40% and 80% rolling reductions). The results from the stringer analysis in Figure 11–Figure 14 and Figure 16–Figure 17 suggest that, in an actual microstructure, as the particle shapes become more elongated and more particles are located along grain boundaries, that microstructure can have larger SVF and greater maximum stringer length with increases of rolling reduction.

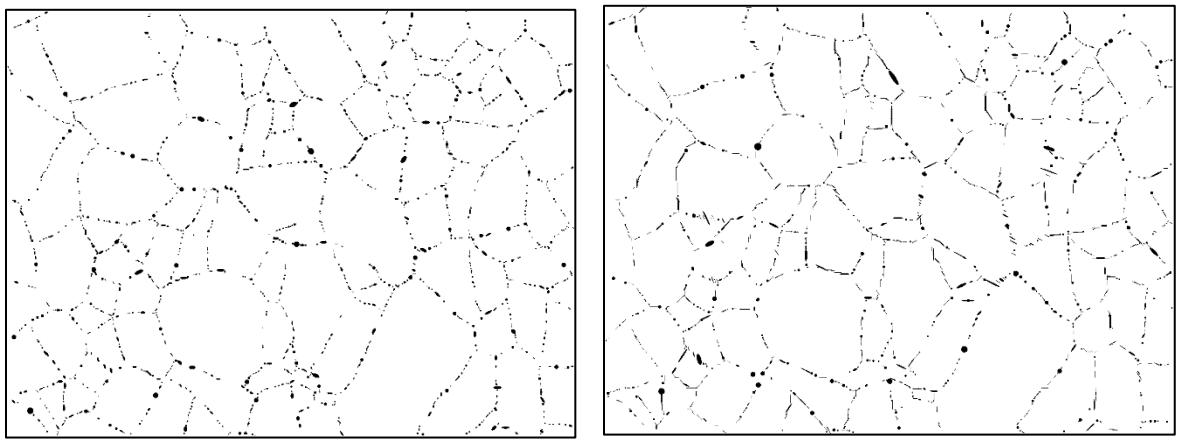

(a) (b)

Figure 15. Examples of synthetic microstructures with different aspect ratios for elliptical particles: (a) aspect ratio of 1~2 and (b) aspect ratio of 1~4.

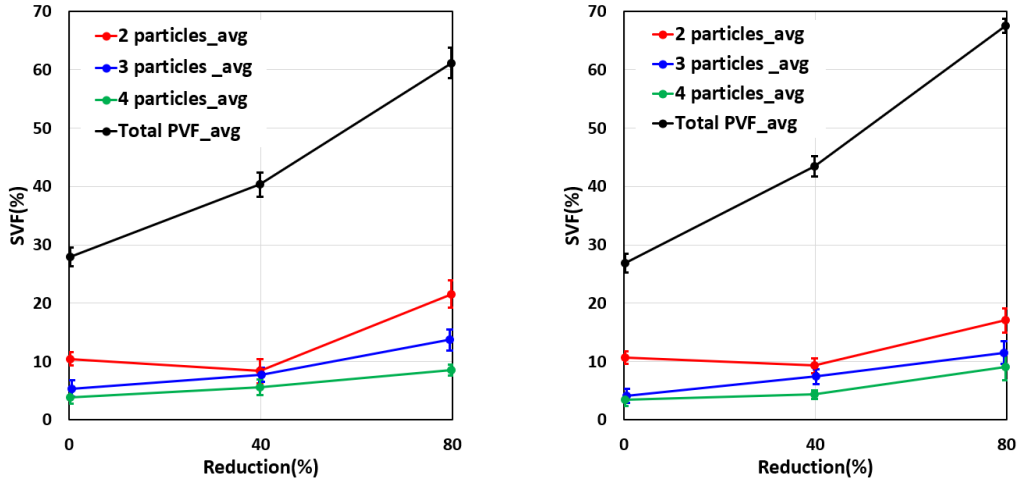

(a) (b)

Figure 16. SVF for particle distributions along grain boundaries: elliptical particles with aspect ratios of (a) 1~2 and (b) 1~4.

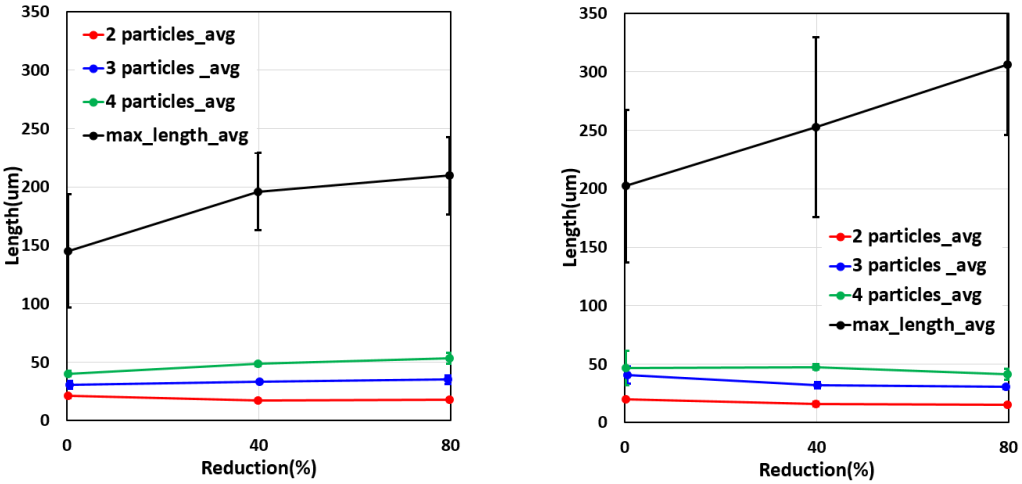

(a) (b)

Figure 17. Maximum stringer length for particle distributions along grain boundaries: elliptical particles with aspect ratios of (a) 1~2 and (b) 1~4.

3.2 Near-Surface Particle Distribution during Hot Rolling

Because carbide particles near the surface can influence the fuel quality and stability, the evolution of particle distributions near the surface was investigated. As a preliminary approach, the number of particles and the PVF near the surface during hot rolling were analyzed. Figure 18 presents a way to obtain the near-surface particle information. As shown in the figure, a depth of 70 μm from the surface was arbitrarily selected to represent near-surface depth, and the same value was used in the deformed microstructures after 40% and 80% rolling reductions. The calculations were performed for both the top and bottom surfaces of all the generated microstructures. For random particle distributions, a distinction is not necessary between the top and bottom surfaces, and the results are based on the average of ten top/bottom near-surface information from five models with the same microstructural features. For particle distribution along grain boundaries, the top and bottom surfaces have different grain-boundary features as shown in Figure 18(b), and the two separate results (i.e., top and bottom) were obtained based on the averages of top and bottom near-surface information from five models. Since the results are quite similar with no noticeable difference between the microstructures with circular particles and those with elliptical particles, only the results for the circular particles are presented in this section.

Figure 19 shows the results for the evolutions of number of particles and PVF near the surface during rolling reduction. Figure 19(a)–Figure 19(c) show the evolution of the near-surface number of particles with increased rolling reduction for the three different overall PVF models (0.5%, 1.0%, 2.0% PVF). The total numbers of particles within the microstructure, which should remain almost constant as presented, are also plotted in the figures as a reference. However, the near-surface number of particles increases with rolling reduction: because the same depth (i.e., 70 μm) value was adopted in calculating the near-surface information for before and after rolling, more of the particles lie within 70 μm depth from the surface although the total thickness has decreased. Interestingly, for all overall PVFs (i.e., 0.5%, 1.0%, and 2.0%), the near-surface number of particles increases by ~80% and ~550% with the 40% and 80% rolling reductions, respectively. Figure 20 shows the evolutions of number of particles at the surface during rolling for the microstructures with circular and elliptical particles. Here, only particles touching the surface are counted as surface particles, regardless of size. As shown in the figure, the number of particles at the surface increases with the increase of rolling reduction and PVF. In counting the number of particles at the surface, a new criterion may need to be developed that considers the particle size and its depth below the surface, because any large particle below the surface may have more substantial interaction with the surface than small particles exposed on the surface have.

Figure 19(d)–Figure 19(f) show the evolution of near-surface PVF with increased rolling reduction for the three different overall PVF models. Total PVFs within the microstructures (i.e., black curves) are also plotted in the figures. As with the total number of particles within the microstructures shown in Figure 19(a)–Figure 19(c), the total PVF should also remain almost constant with increased rolling reduction, because the materials in this study are considered incompressible. However, in Figure 19(d)–Figure 19(f), the total PVF increases by ~5% and ~15% from the initial PVF with the 40% and 80% rolling reductions, respectively. This is probably due to a slight increase of PVF that may have been introduced in error during the remeshing process after each rolling simulation. Therefore, the results in Figure 19(d)–Figure 19(f) are to be analyzed with these errors considered, and the actual near-surface PVF values (i.e., red and blue curves) for 40% and 80% rolling reductions are to be slightly decreased from those presented in the figures. From the figures, the near-surface PVF prior to rolling may be different from (usually lower than) the given overall PVF. However, the near-surface PVF changes (usually increases slightly) and approaches the given overall PVF with increased rolling reduction. In order to accurately calculate the near-surface information, a new remeshing code needs to be developed that does not change the overall PVF. Near-surface SVF would also be interesting to investigate in future work.

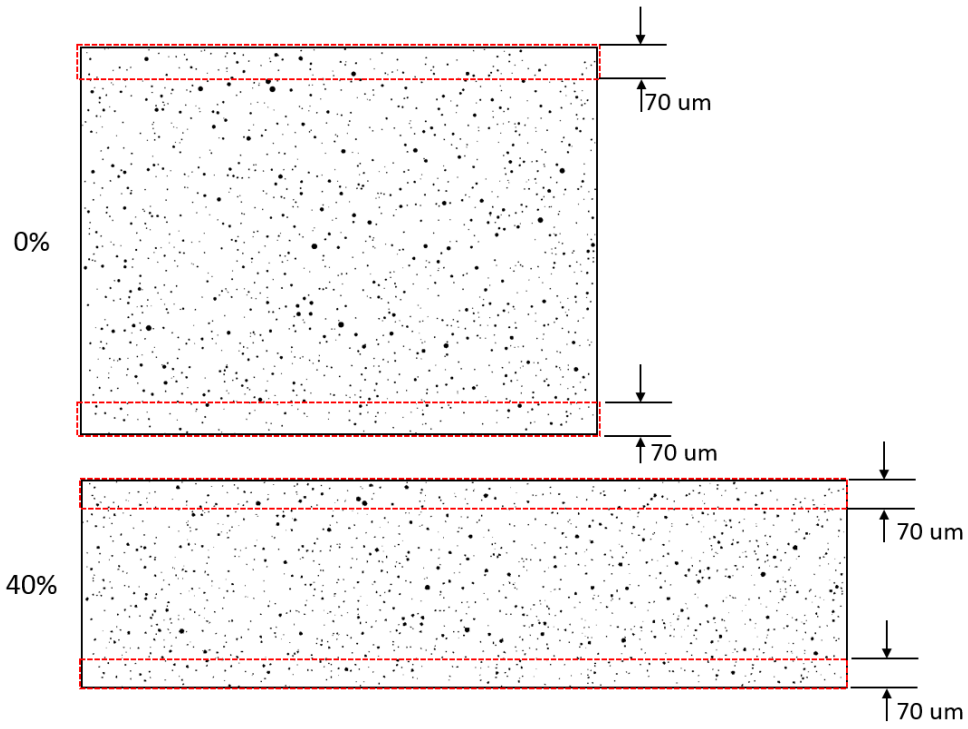

(a)

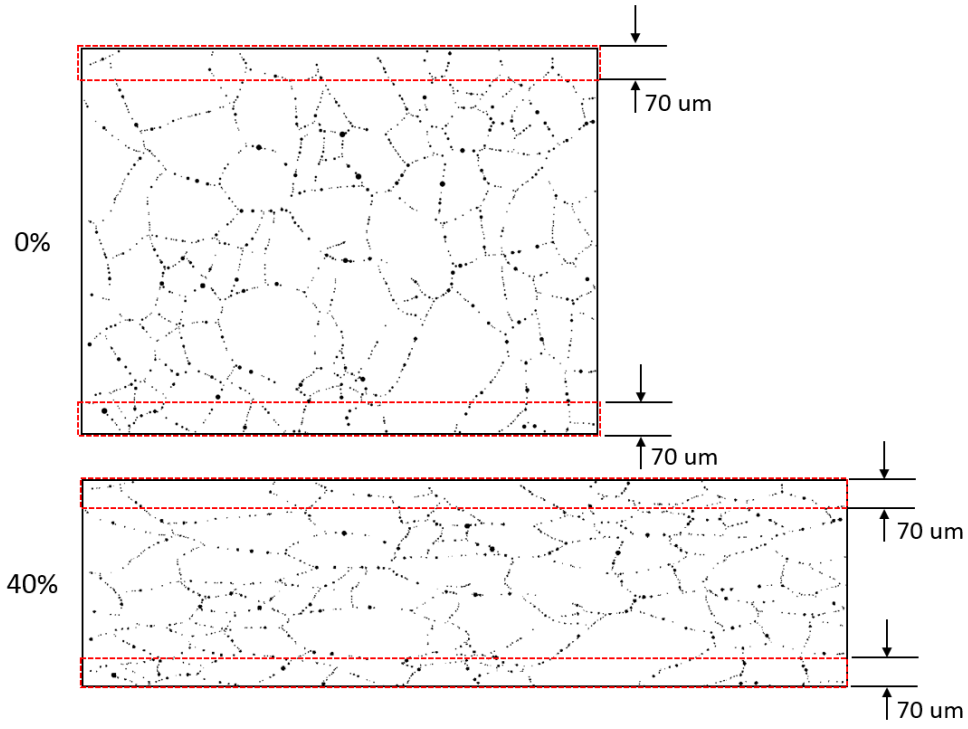

(b)

Figure 18. Schematics for near-surface particle information: (a) model for random particle distribution; (b) model for particle distribution along grain boundaries.

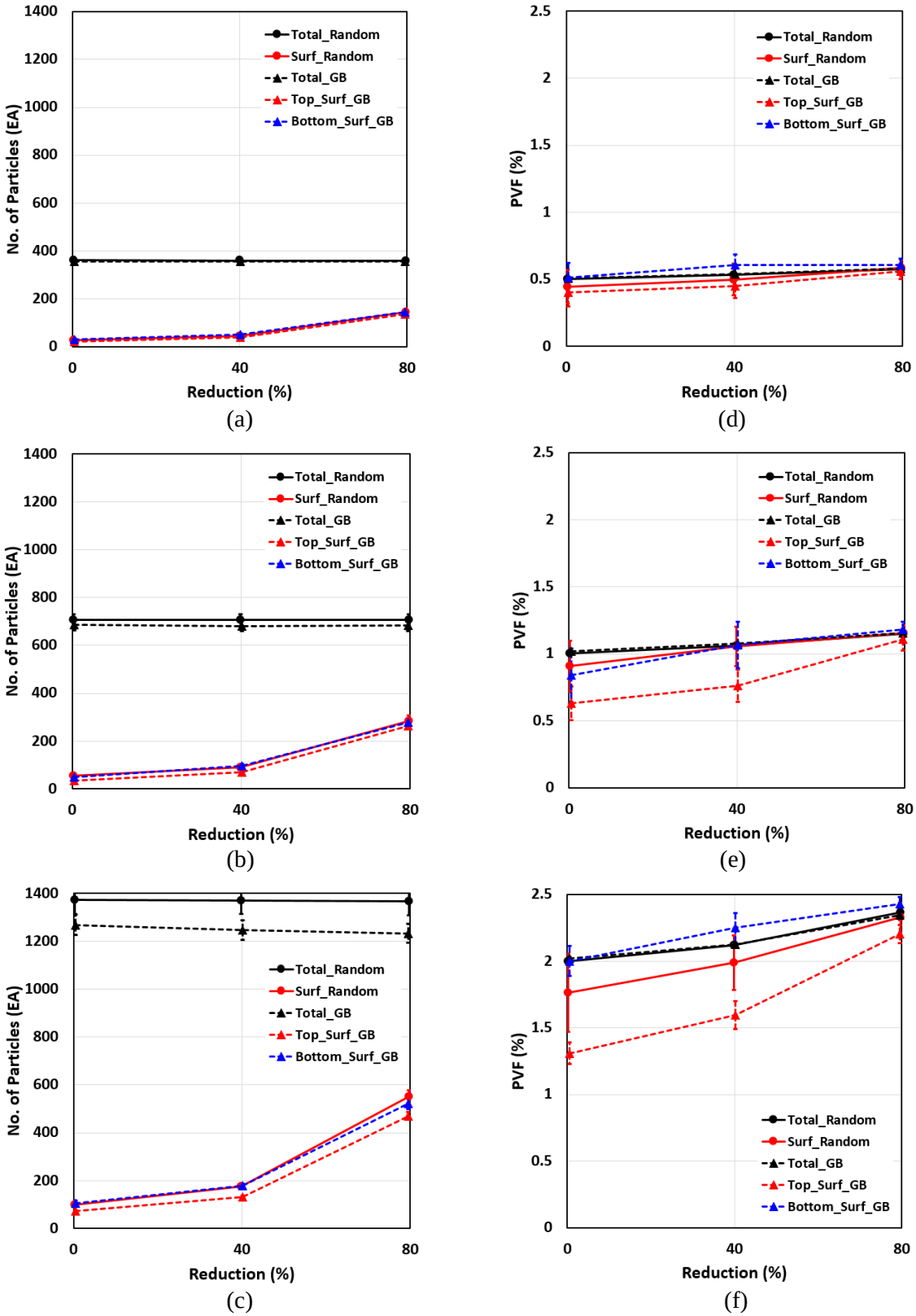

Figure 19. Evolution of near-surface number of particles and PVF during rolling: (a), (b), (c) number of near-surface particles for 0.5%, 1.0%, and 2.0% PVF models, respectively; (d), (e), (f) near-surface PVF for 0.5%, 1.0%, and 2.0% PVF models, respectively.

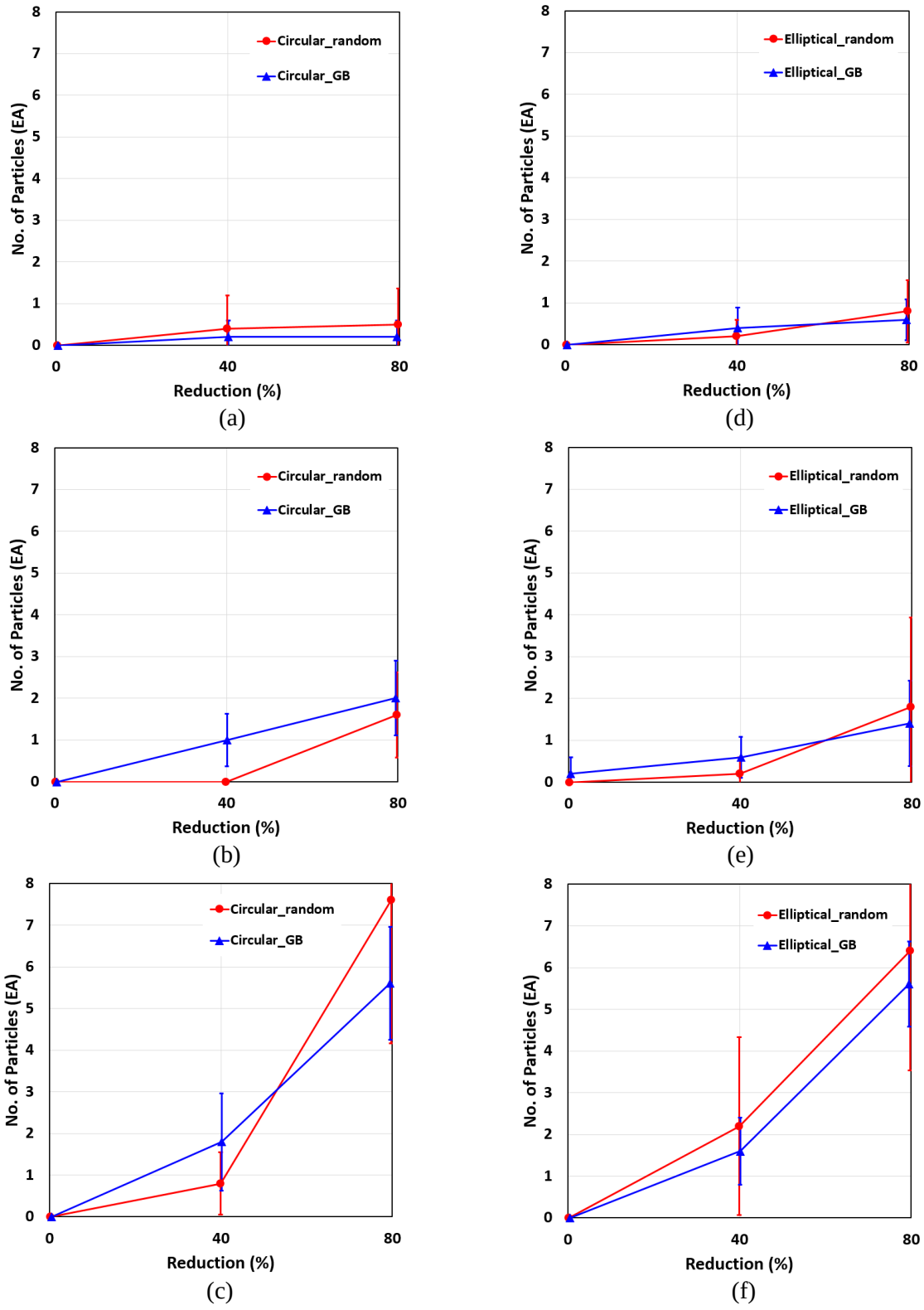

Figure 20. Evolution of number of particles at the surface during rolling: (a), (b), (c) number of particles on the surface for the microstructures with circular particles with 0.5%, 1.0%, and 2.0% PVF, respectively; (d), (e), (f) number of particles at the surface for the microstructures with elliptical particles with 0.5%, 1.0%, and 2.0% PVF, respectively.

4.0 Conclusions

The influence of initial carbide particle distribution features on the evolution of particle and stringer distribution within U-10Mo alloy during hot rolling was investigated in this study. Various synthetic microstructure-based FE models were generated with consideration of different parameters: (1) particle shapes (circular and elliptical), (2) particle volume faction (PVF) (0.5, 1.0, and 2.0 %), and (3) particle distributions (random and along grain boundaries). Plane-strain compression loading was applied to the FE models to simulate the hot rolling process to 40% and 80% reductions. Stringer statistics analyses and two-point correlation functions (2PCF) were then performed with the simulation results. Some key results from the stringer statistics analyses are summarized below, and the results from the 2PCF are in Appendix section.

1. With increased rolling reduction, the SVF generally remains the same for microstructures with random particle distributions and substantially increases for particle distributions along grain boundaries: by ~50% and ~100% with the 40% and 80% rolling reductions, respectively. Here, the rate of increase of the SVF (i.e., increment of SVF(%)/increment of rolling reduction(%)) can be higher for higher PVF. For 0.5%, 1.0%, and 2.0% PVF, the rate of increase of the SVF was calculated as ~0.1, ~0.2, and ~0.4, respectively.
2. SVF for microstructures with elliptical particles can be slightly higher (about 5~10% higher for the 40~80% rolling reduction) than for those with circular particles.
3. Maximum stringer length can be higher for higher PVF. Maximum stringer length substantially increases with increased rolling reduction (by about 30~50% for the 40~80% rolling reduction) for the microstructures with elliptical particles along grain boundaries. For other microstructural features (i.e., random particle distribution with circular/elliptical particles, and particle distribution along grain boundaries with circular particles), the increase of maximum stringer length with the rolling reduction is less significant (by about 5~30% for the 40~80% rolling reduction).
4. The SVF and maximum stringer length can become larger as the aspect ratio of the elliptical particles increases.
5. The number of near-surface particles increases by ~80% and ~550% with the 40% and 80% rolling reductions, respectively.
6. Near-surface PVF prior to rolling may be different from the given overall PVF. With increased rolling reduction, it can change slightly and approach the given overall PVF.

Based on the developed synthetic microstructures, cold rolling simulations after 80% hot rolling reduction are currently underway. Particle evolutions and fractures after cold rolling will be investigated as future work.

5.0 References

1. Burkes, D.E., Prabhakaran, R., Hartmann, T., Jue, J.-F. and Rice, F.J., "Properties of DU–10wt% Mo alloys subjected to various post-rolling heat treatments." *Nuclear Engineering and Design*, 2010. **240**(6):1332-1339.
2. Meyer, M.K., Hofman, G.L., Hayes, S.L., Clark, C.R., Wiencek, T.C., Snelgrove, J.L., Strain, R.V. and Kim, K.-H., "Low-temperature irradiation behavior of uranium–molybdenum alloy dispersion fuel." *Journal of Nuclear Materials*, 2002. **304**(2): 221-236.
3. Snelgrove, J.L., Hofman, G.L., Meyer, M.K., Trybus, C.L. and Wiencek, T.C., "Development of very-high-density low-enriched-uranium fuels." *Nuclear Engineering and Design*, 1997. **178**(1):119-126.
4. Sease, J., Primm III, R. and Miller, J., *Conceptual process for the manufacture of low-enriched uranium/molybdenum fuel for the high flux isotope reactor*. ORNL/TM-2007/39, 2007, Oak Ridge National Laboratory (ORNL), Oak Ridge, TN (US).
5. Wachs, D.M., Clark, C.R. and Dunavant, R.J., *Conceptual process description for the manufacture of low-enriched uranium-molybdenum fuel*. 2008, Idaho National Laboratory Report INL/EXT-08-13840.
6. Xu, Z., Joshi, V., Hu, S., Paxton, D., Lavender, C. and Burkes, D., "Modeling the homogenization kinetics of as-cast U-10wt% Mo alloys." *Journal of Nuclear Materials*, 2016. **471**:154-164.
7. Devaraj, A., Joshi, V.V., Prabhakaran, R., Hu, S.Y., McGarrah, E.J. and Lavender, C.A., *Theoretical Model for Volume Fraction of UC, 235U Enrichment, and Effective Density of Final U 10Mo Alloy*. 2016, PNNL-SA-117284, Pacific Northwest National Laboratory (PNNL), Richland, WA (US).
8. Soulami, A., Burkes, D.E., Joshi, V.V., Lavender, C.A. and Paxton, D., "Finite-element model to predict roll-separation force and defects during rolling of U-10Mo alloys." *Journal of Nuclear Materials*, 2017. **494**:182-191.
9. Jana, S., Devaraj, A., Kovarik, L., Arey, B., Sweet, L., Varga, T., Lavender, C. and Joshi, V., "Kinetics of cellular transformation and competing precipitation mechanisms during sub-eutectoid annealing of U10Mo alloys." *Journal of Alloys and Compounds*, 2017. **723**:757-771.
10. Cheng, G., Hu, X., Frazier, W.E., Lavender, C.A. and Joshi, V.V., "Effect of second phase particles and stringers on microstructures after rolling and recrystallization." *Materials Science and Engineering: A*, 2018. **736**:41-52.
11. Hannard, F., Castin, S., Maire, E., Mokso, R., Pardoen, T. and Simar, A., "Ductilization of aluminium alloy 6056 by friction stir processing." *Acta Materialia*, 2017. **130**:121-136.
12. Hu, X., Wilkinson, D.S., Jain, M. and Mishra, R.K., "The influence of particle shape, volume fraction and distribution on post-necking deformation and fracture in uniaxial tension of AA5754 sheet materials." *International Journal of Solids and Structures*, 2009. **46**(13):2650-2658.
13. Hu, X., Wilkinson, D.S., Jain, M. and Mishra, R.K., "A parametric finite element study and an analytical model of particle distributions on post-necking deformation and failure mode in AA5754 aluminum alloy sheets." *International Journal of Fracture*, 2010. **164**(2):167-183.
14. Hu, X., Wilkinson, D.S., Jain, M., Wu, P. and Mishra, R.K., "The impact of particle distributions and grain-level inhomogeneities on post-necking deformation and fracture in AA5754 sheet alloys during uniaxial tension." *Materials Science and Engineering: A*, 2011. **528**(4):2002-2016.
15. Allison, J., Backman, D. and Christodoulou, L., "Integrated computational materials engineering: a new paradigm for the global materials profession." *JOM*, 2006. **58**(11):25-27.
16. Hu, S., Burkes, D., Lavender, C.A. and Joshi, V.V., "Effect of grain morphology on gas bubble swelling in UMo fuels – A 3D microstructure dependent Booth model." *Journal of Nuclear Materials*, 2016. **480**:323-331.
17. Joshi, V.V., Nyberg, E.A., Lavender, C.A., Paxton, D. and Burkes, D.E., "Thermomechanical process optimization of U-10wt% Mo – Part 1: high-temperature compressive properties and microstructure." *Journal of Nuclear Materials*, 2015. **465**:805-813.

18. Joshi, V.V., Nyberg, E.A., Lavender, C.A., Paxton, D. and Garmestani, H., "Thermomechanical process optimization of U-10wt% Mo – Part 2: The effect of homogenization on the mechanical properties and microstructure." *Journal of Nuclear Materials*, 2015. **465**:710-718.
19. Nyberg, E.A., Joshi, V.V., Lavender, C.A., Paxton, D.A. and Burkes, D., *The Influence of Casting Conditions on the Microstructure of As-Cast U-10Mo Alloys: Characterization of the Casting Process Baseline*. 2013, PNNL-23049, Pacific Northwest National Laboratory (PNNL), Richland, WA (US).
20. Wang, X., Xu, Z., Wang, C., Soulami, A., Frazier, W., Cheng, G., Hu, X. and Hu, S., *Process Modeling of U-10wt% Mo Alloys Using Integrated Computational Materials Engineering*. (In preparation), Pacific Northwest National Laboratory (PNNL), Richland, WA (US).
21. Joshi, V.V., Paxton, D.M., Lavender, C.A. and Burkes, D.E., *The Effect of Rolling As-Cast and Homogenized U-10Mo Samples on the Microstructure Development and Recovery Curves*. 2016, PNNL-25781, Pacific Northwest National Laboratory (PNNL), Richland, WA (US).
22. ASTM E45-05. 2005. *Standard Test Methods for Determining the Inclusion Content of Steel*. ASTM International, West Conshohocken, PA. Available at www.astm.org.
23. Hu, X., Wang, X., Joshi, V.V. and Lavender, C.A., "The effect of thermomechanical processing on second phase particle redistribution in U-10wt%Mo." *Journal of Nuclear Materials*, 2017. **500**:270-279.

Appendix A

Two-Point Correlation Functions

The 2PCF is defined in this section. The 2PCF method is one of the most important statistical descriptors of microstructure for heterogeneous materials [20, 23]. For a two-phase material, the 2PCF is defined as

$$S_2^{(i)}(\boldsymbol{x}_1, \boldsymbol{x}_2) = \left\langle I^{(i)}(\boldsymbol{x}_1) I^{(i)}(\boldsymbol{x}_2) \right\rangle, \tag{7}$$

where i denotes the two phases ($i = 1, 2$), $\boldsymbol{x}_1$ and $\boldsymbol{x}_2$ are two randomly chosen points, $I^{(i)}(\boldsymbol{x})$ is an indicator function, and the angular brackets $\langle \cdots \rangle$ denote ensemble averaging over the random medium. The indicator function $I^{(i)}(\boldsymbol{x})$ is defined as

$$I^{(i)}(x) = \begin{cases} 1, & \boldsymbol{x} \in \boldsymbol{V}_i, \\ 0, & \boldsymbol{x} \in \overline{\boldsymbol{V}}_i, \end{cases} \tag{8}$$

where V_i represents the region of phase i and $\overline{V}_i$ is the region occupied by the other phase.

For the specific application in this study, the 2PCF is calculated to quantify the spatial distribution of carbides. Consider a vector $\boldsymbol{r}^{\theta} = (r, \theta)$ with length r and angle θ randomly thrown into the microstructure as in Figure 21. The 2PCF in this study records the occurrence when the two ends ($\boldsymbol{x}_i$ and $\boldsymbol{x}_i + \boldsymbol{r}^{\theta}$) of the vector $\boldsymbol{r}$ land inside two different carbide particles using the following expression:

$$S_2^{(p)}(\mathbf{r}) = \sum_{i=1}^{N} I^{(p)}(\mathbf{x}_i) I^{(p)}(\mathbf{x}_i + \mathbf{r}) \tag{9}$$

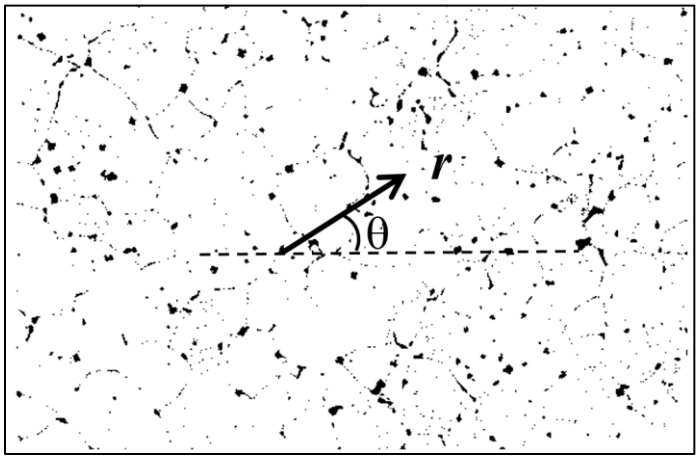

Figure 21. A vector $\boldsymbol{r}$ with length r and angle θ in a microstructure domain.

In Figure 21, the microstructure domains are elongated along the horizontal direction by rolling, yielding increased horizontal distance between particles after thickness reduction. Along the thickness direction, the domains are compressed by rolling, and the particles become vertically much closer to each other. In this study, the 2PCFs of the microstructures are only calculated on horizontal and vertical directions. To have sufficient data, the vertical direction is defined as a range of ±15° around $\theta = 90°$, and the horizontal direction is defined as a range of ±15° around $\theta = 0°$. Here, the remeshed microstructure data after 40% and 80% rolling reductions (i.e., 1967 × 532 pixels and 5785 × 178 pixels, respectively) were used for these calculations.

Figure 22–Figure 25 show the calculated 2PCFs of the models with different microstructural features for horizontal (i.e., rolling) and vertical (i.e., normal) directions as the rolling reduction increases. Each figure shows the evolution of the 2PCF of two models with the same microstructural features. For example, the solid curves represent the evolution of the functions for one microstructure, whereas the dotted curves represent those of the other microstructure. The figures here are not to show the calculated absolute values of the 2PCF, but to show the shape evolution of the functions with the increase of rolling reduction. Therefore, the curves in the figures were shifted along the vertical axis in order to avoid overlap of the curves and then to compare the curve shapes.

For the vertical direction, as in Figure 23 and Figure 25, the 2PCF curves shrink in the direction of the *r* axis as the rolling reduction increases. For example, see the red curves in Figure 23 and Figure 25. Their limited extent in the direction of the *r* axis implies that the domain of analysis is reduced due to the thickness reduction. For a similar reason, along the horizontal direction, the 2PCF curves expand in the direction of the *r* axis with the increase of rolling reduction, although this expansion is not presented in Figure 22 and Figure 24. These expansions result from the elongation of the domain in the horizontal direction. A detailed analysis on the evolution of peaks of the 2PCF curves with the progressive increase of rolling reduction from 0% to 60% can be found in a previous report [20]. The evolution of peaks is not to be traced in this study, as the amount of rolling reduction at a time is rather large (i.e., 40%).

The influence of different microstructural features on their 2PCF curves is of more interest in this study. First, in Figure 22–Figure 25, the graphs in the left column (for circular particles) can be compared with the corresponding graphs in the right column (for elliptical particles) to examine the influence of particle shape. Note that, as mentioned above, the microstructures with elliptical particles have exactly the same particle distribution (i.e., location) as that of the corresponding microstructures with circular particles (see Figure 5 and Figure 6). Therefore, as compared in the figures, overall curve shapes for the microstructures with circular particles are quite similar to those with elliptical particles. In general, they only differ slightly in the values of peaks and valleys of the curves. This slight difference is considered to be the effect of particle shape; it can also depend on the aspect ratio of the elliptical particles. Second, as the PVF increases, the values of 2PCF increase due to the greater chance that the two ends of the vector $\boldsymbol{r}$ in Equation ($S_2^{(p)}\left(\mathbf{r}\right) = \sum_{i=1}^{N} I^{(p)}\left(\mathbf{x}_i\right) I^{(p)}\left(\mathbf{x}_i + \mathbf{r}\right)$ (9) land inside two different particles. Also, for the higher PVF, the curves tend to show more peaks in general and to have higher peaks at short distance. Third, from comparison of Figure 22 and Figure 24, it can be seen that the curves for microstructures with particles distributed along grain boundaries tend to show higher peaks at short distance, which then gradually decrease as the distance increases. Note that, for the microstructures with particle distributions along grain boundaries, the particles are more likely to have neighboring particles nearby along the grain boundary (especially for the microstructures with higher PVF) than microstructures with random particle distributions.

Key results from the 2PCF are summarized below.

1. Overall shapes of the 2PCF curves are quite similar in the microstructures with circular and elliptical particles. They only differ in the values of peaks and valleys of the curves, which is an effect of particle shape.
2. For higher PVF, the 2PCF curves tend to show more peaks and to have higher peaks at short distance. The values of correlation curves are also higher for higher PVF.
3. The 2PCF curves for the microstructures with particle distributions along grain boundaries tend to show higher peaks at short distance than those for random particle distributions, which then gradually decrease as the distance increases.

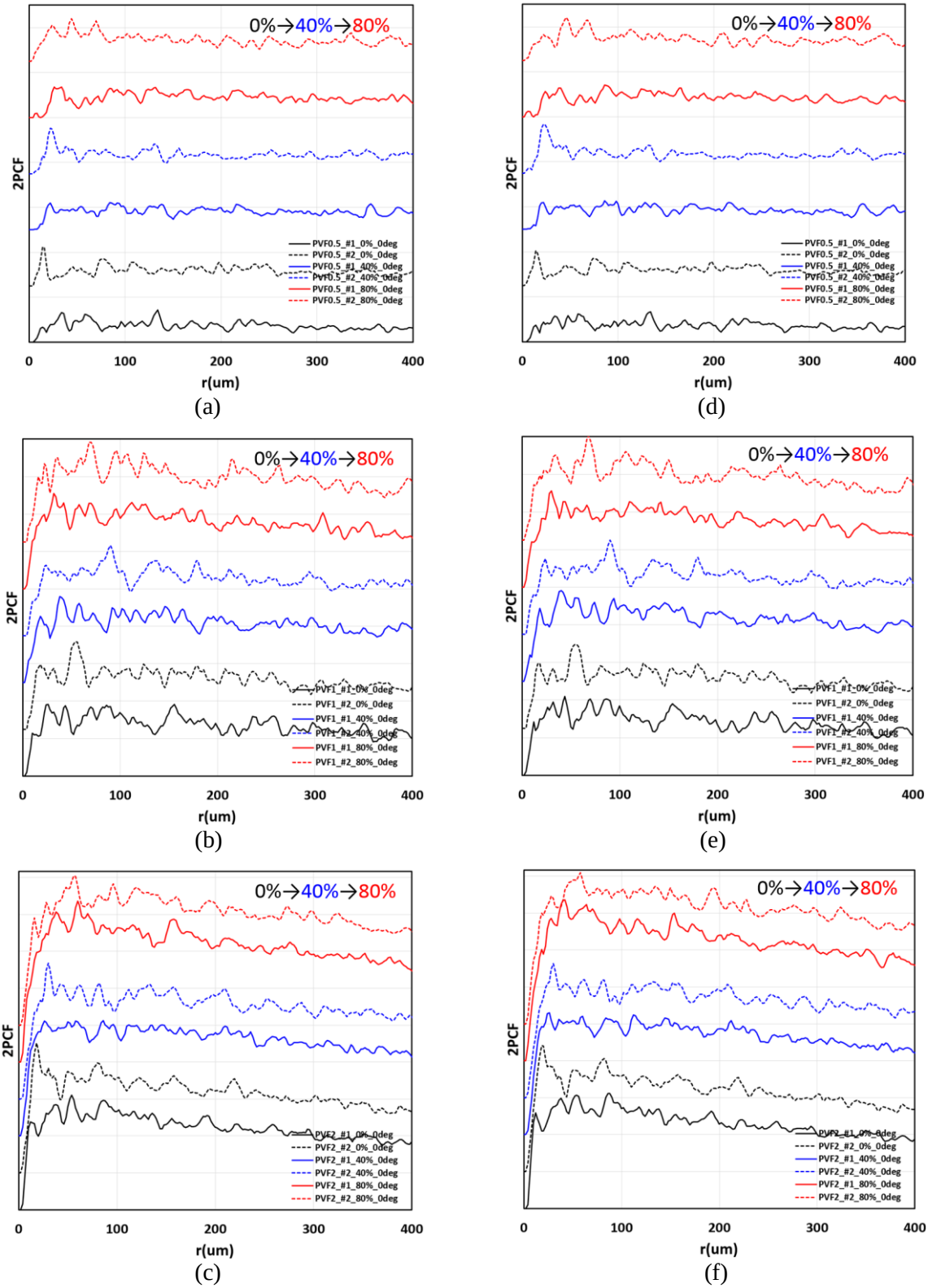

Figure 22. 2PCF curves in the rolling (θ = 0°) direction for random particle distributions: (a), (b), (c) circular particles with 0.5%, 1.0%, and 2.0% PVF, respectively, and (d), (e), (f) elliptical particles with 0.5%, 1.0%, and 2.0% PVF, respectively.

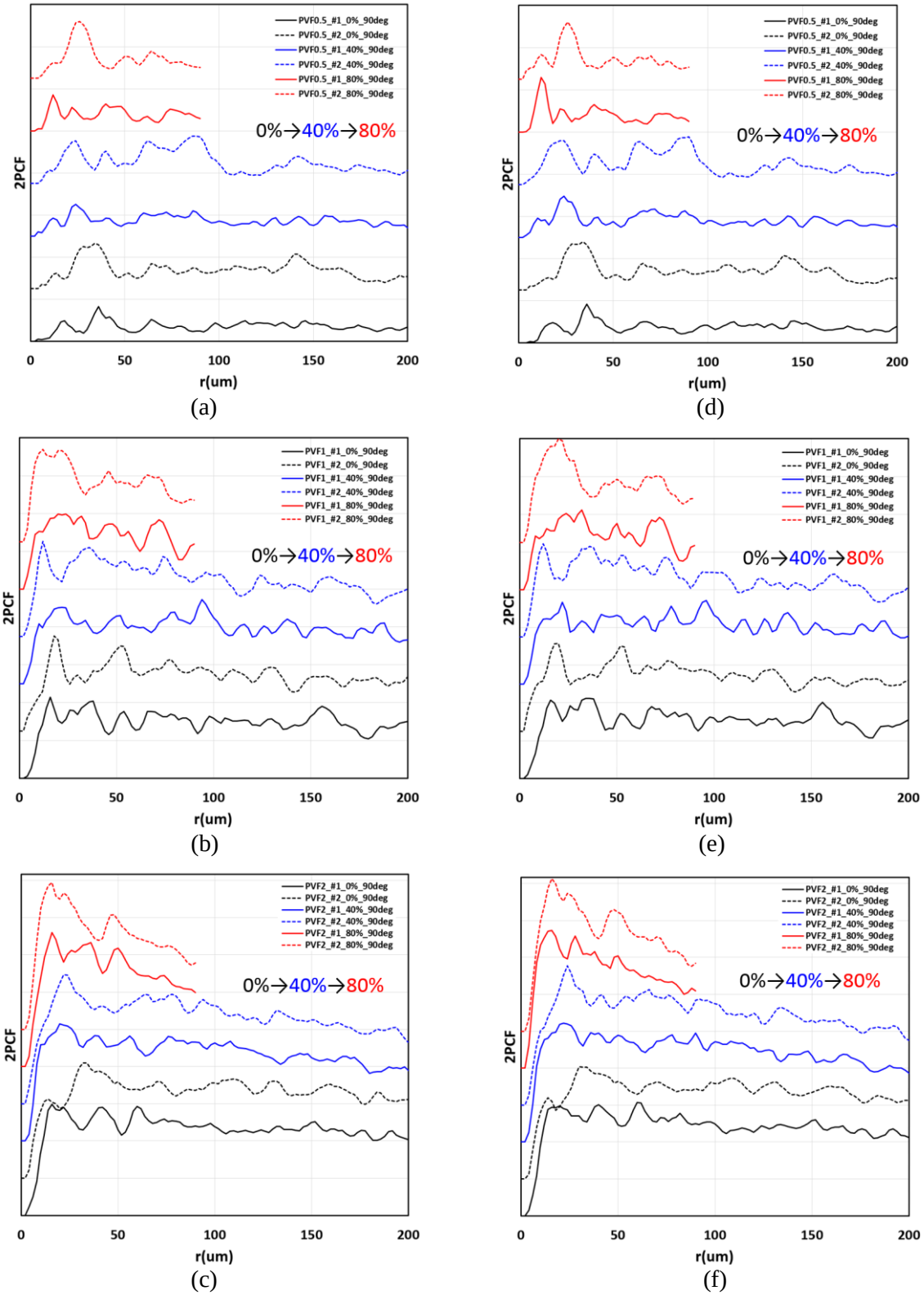

Figure 23. 2PCF curves in the normal (θ = 90°) direction for random particle distributions: (a), (b), (c) circular particles with 0.5%, 1.0%, and 2.0% PVF, respectively, and (d), (e), (f) elliptical particles with 0.5%, 1.0%, and 2.0% PVF, respectively.

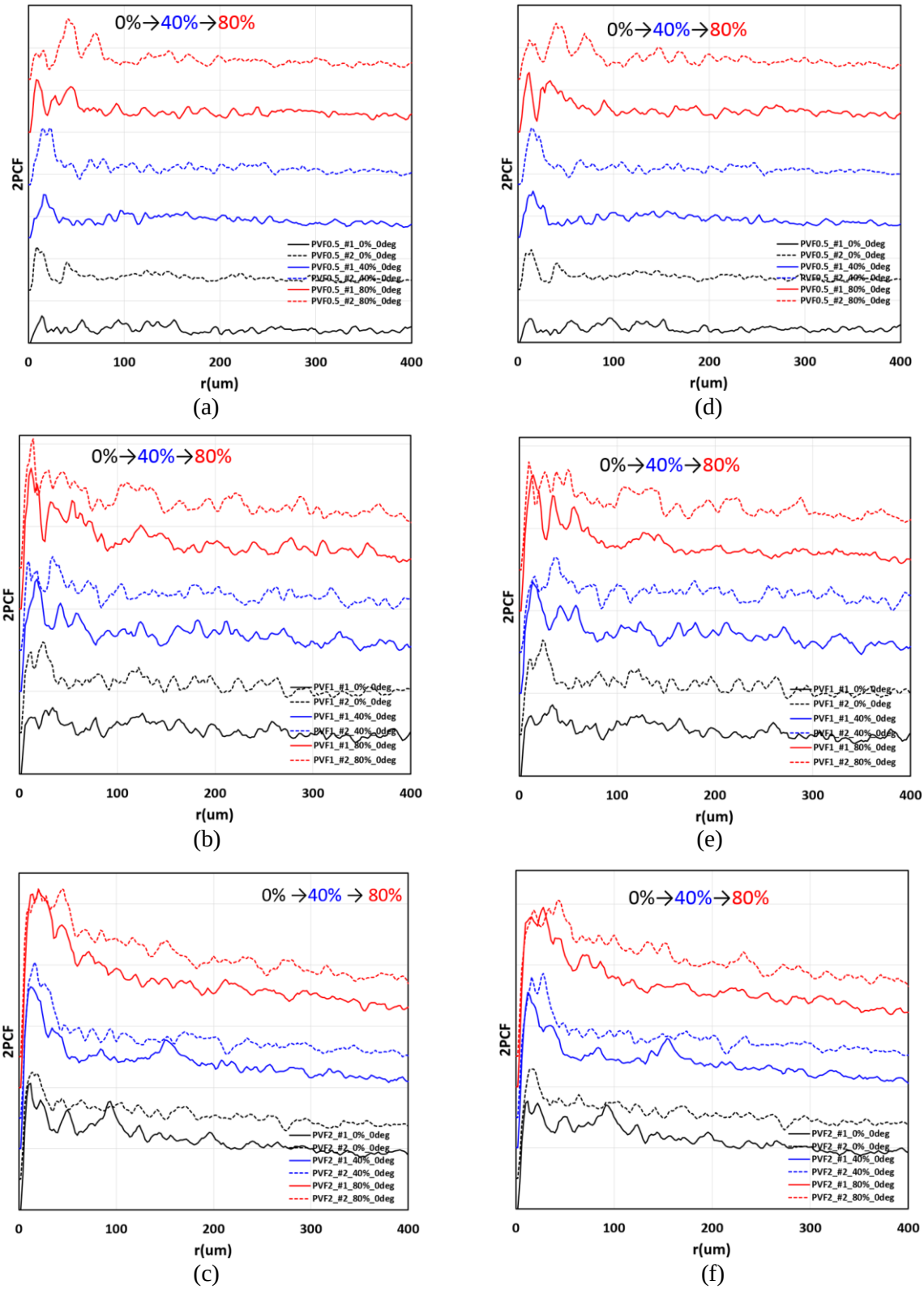

Figure 24. 2PCF curves in the rolling (θ = 0°) direction for particle distributions along grain boundaries: (a), (b), (c) circular particles with 0.5%, 1.0%, and 2.0% PVF, respectively, and (d), (e), (f) elliptical particles with 0.5%, 1.0%, and 2.0% PVF, respectively.

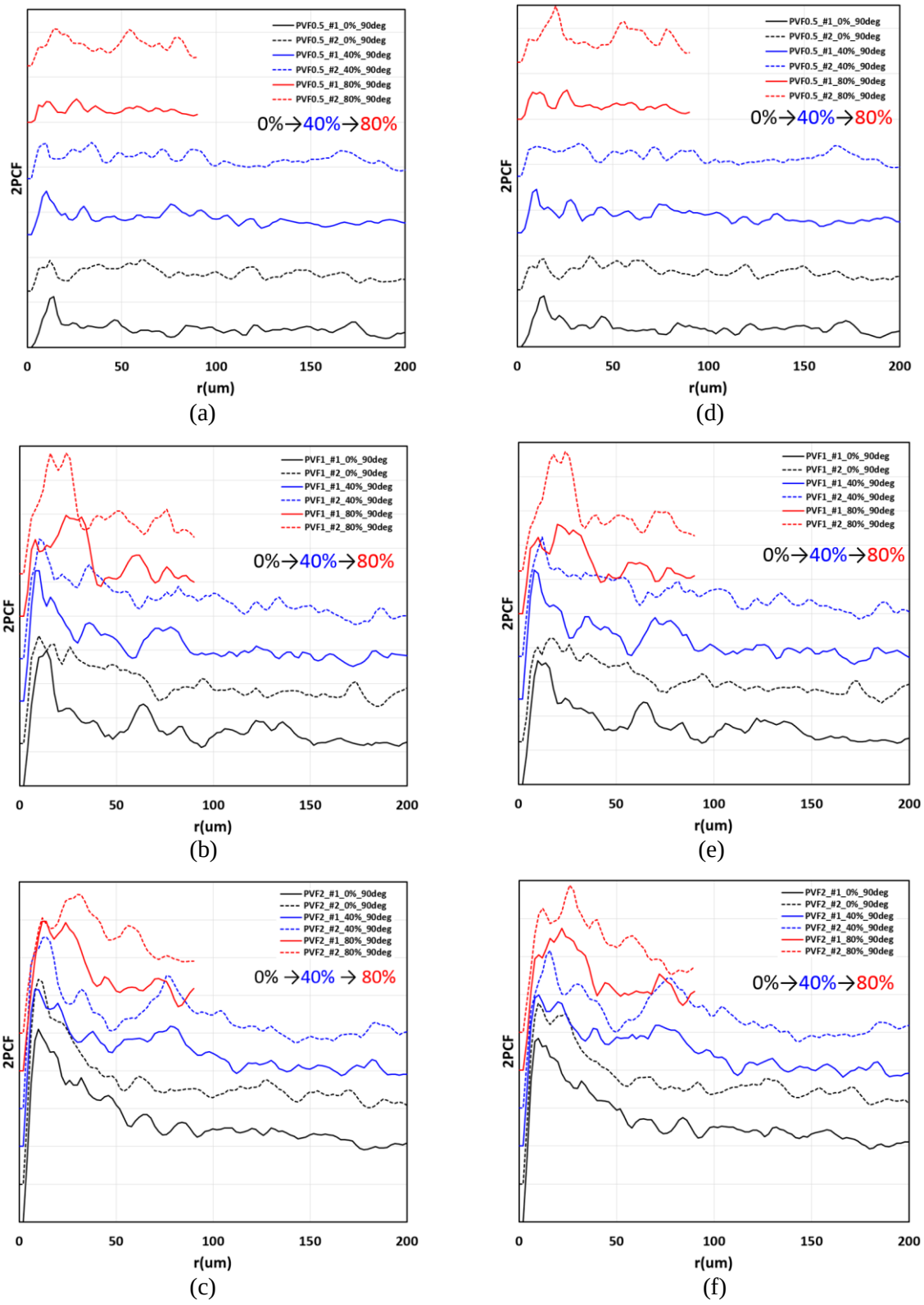

Figure 25. 2PCF curves in the normal (θ = 90°) direction for particle distributions along grain boundaries: (a), (b), (c) circular particles with 0.5%, 1.0%, and 2.0% PVF, respectively, and (d), (e), (f) elliptical particles with 0.5%, 1.0%, and 2.0% PVF, respectively.

Pacific Northwest
NATIONAL LABORATORY

Proudly Operated by **Battelle** *Since 1965*

U.S. DEPARTMENT OF
ENERGY

902 Battelle Boulevard
P.O. Box 999
Richland, WA 99352
1-888-375-PNNL (7665)

www.pnnl.gov